

# Cyanopolyyne line survey towards high-mass star-forming regions with TMRT

Y. X. Wang (汪友鑫)<sup>1</sup>, J. S. Zhang (张江水)<sup>1,★</sup>, Y. T. Yan (闫耀庭)<sup>2,★★</sup>, J. J. Qiu (邱建杰)<sup>3</sup>, J. L. Chen(陈家梁)<sup>1</sup>, J. Y. Zhao(赵洁瑜)<sup>1</sup>, Y. P. Zou(邹益鹏)<sup>1</sup>, X. C. Wu(吴贤聪)<sup>1</sup>, X. L. He(何晓玲)<sup>1</sup>, Y. B. Gong(龚宇彬)<sup>1</sup>, J. H. Cai(蔡嘉华)<sup>1</sup>

<sup>1</sup> Centre For Astrophysics, Guangzhou University, Guangzhou 510006, PR China

<sup>2</sup> Max-Planck-Institut für Radioastronomie, Auf dem Hügel 69, D-53121 Bonn, Germany

<sup>3</sup> School of Physics and Astronomy, Sun Yat-sen University, Guangzhou 510275, PR China

## ABSTRACT

**Context.** Cyanopolyynes ( $\text{HC}_{2n+1}\text{N}$ ,  $n = 1,2,3$ ), which are the linear carbon chain molecules, are precursors for the prebiotic synthesis of simple amino acids. They are important for understanding prebiotic chemistry and may be good tracers of the star formation sequence.

**Aims.** We aim to search for cyanopolyynes in high-mass star-forming regions (HMSFRs) at possibly different evolutionary stages, investigate the evolution of  $\text{HC}_3\text{N}$  and its relation with shock tracers, and detect the existence of  $\text{HC}_5\text{N}$  and  $\text{HC}_7\text{N}$  in HMSFRs with a formed protostar.

**Methods.** We carried out a cyanopolyyne line survey towards a large sample of HMSFRs using the Shanghai Tian Ma 65m Radio Telescope (TMRT). Our sample consisted of 123 targets taken from the TMRT C band line survey. It included three kinds of sources, namely those with detection of the 6.7 GHz  $\text{CH}_3\text{OH}$  maser alone, with detection of the radio recombination line (RRL) alone, and with detection of both (hereafter referred to as Maser-only, RRL-only, and Maser-RRL sources, respectively). For our sample with detection of cyanopolyynes, their column densities were derived using the rotational temperature measured from the  $\text{NH}_3$  lines. We constructed and fitted the far-infrared (FIR) spectral energy distributions (SED; obtained from the Herschel FIR data and the Atacama Pathfinder Experiment data at 870  $\mu\text{m}$ ) of our  $\text{HC}_3\text{N}$  sources. Moreover, by analysing the relation between  $\text{HC}_3\text{N}$  and other shock tracers, we also investigate whether  $\text{HC}_3\text{N}$  is a good tracer of shocks.

**Results.** We detected  $\text{HC}_3\text{N}$  in 38 sources,  $\text{HC}_5\text{N}$  in 11 sources, and  $\text{HC}_7\text{N}$  in G24.790+0.084, with the highest detection rate being found for Maser-RRL sources and a very low detection rate found for RRL-only sources. The mean column density of  $\text{HC}_3\text{N}$  was found to be  $(1.75 \pm 0.42) \times 10^{13}$ ,  $(2.84 \pm 0.47) \times 10^{13}$ , and  $(0.82 \pm 0.15) \times 10^{13}$   $\text{cm}^{-2}$  for Maser-only, Maser-RRL, and RRL-only sources, respectively. Based on a fit of the FIR SED, we derive their dust temperatures,  $\text{H}_2$  column densities, and abundances of cyanopolyynes relative to  $\text{H}_2$ . The mean relative abundance of  $\text{HC}_3\text{N}$  was found to be  $(1.22 \pm 0.52) \times 10^{-10}$  for Maser-only,  $(5.40 \pm 1.45) \times 10^{-10}$  for Maser-RRL, and  $(1.65 \pm 1.50) \times 10^{-10}$  for RRL-only sources, respectively.

**Conclusions.** The detection rate, the column density, and the relative abundance of  $\text{HC}_3\text{N}$  increase from Maser-only to Maser-RRL sources and decrease from Maser-RRL to RRL-only sources. This trend is consistent with the proposed evolutionary trend of  $\text{HC}_3\text{N}$  under the assumption that our Maser-only, Maser-RRL, and RRL-only sources correspond to massive young stellar objects, ultra-compact  $\text{HII}$  regions, and normal classical  $\text{HII}$  regions, respectively. Our detections enlarge the sample of  $\text{HC}_3\text{N}$  in HMSFRs and support the idea that unsaturated complex organic molecules can exist in HMSFRs with a formed protostar. Furthermore, a statistical analysis of the integrated line intensity and column density of  $\text{HC}_3\text{N}$  and shock-tracing molecules ( $\text{SiO}$ ,  $\text{H}_2\text{CO}$ ) enabled us to find positive correlations between them. This suggests that  $\text{HC}_3\text{N}$  may be another tracer of shocks, and should therefore be the subject of further observations and corresponding chemical simulations. Our results indirectly support the idea that the neutral–neutral reaction between  $\text{C}_2\text{H}_2$  and  $\text{CN}$  is the dominant formation pathway of  $\text{HC}_3\text{N}$ .

**Key words.** astrochemistry – stars:formation – ISM:clouds – ISM: molecules

## 1. Introduction

Molecules have been detected in space in various environments, including star-forming regions, the envelopes around evolved stars, well-developed protoplanetary discs around stars, and even distant galaxies. They serve as a useful probe of the physical conditions of their environments, and can be used to derive the ages

of their natal molecular cloud (Herbst & van Dishoeck 2009; Jørgensen et al. 2020; Gerner et al. 2014; Sabatini et al. 2021; Gieser et al. 2021). So far, around 250 molecules have been detected in the interstellar medium and circumstellar shells<sup>1</sup>. Among them, carbon chain molecules contribute a very large portion of the known chemical complexity of the interstellar medium (Thaddeus & McCarthy 2001; Loomis et al. 2016; Law et al. 2018). As typical linear carbon chain molecules, cyanopolyynes ( $\text{HC}_{2n+1}\text{N}$ ,  $n = 1,2,3,\dots$ ) have attracted great interest from astronomers in both observational studies and labora-

<sup>★</sup> e-mail: jszhang@gzhu.edu.cn

<sup>★★</sup> Member of the International Max Planck Research School (IMPRS) for Astronomy and Astrophysics at the universities of Bonn and Cologne.

<sup>1</sup> <https://cdms.astro.uni-koeln.de/classic/molecules>

tory theoretical works (e.g. Travers et al. 1996; Bell et al. 1997; McCarthy et al. 1998; Loomis et al. 2016; Cernicharo et al. 2020). Due to their nitrile bond (-C≡N), cyanopolyyynes are considered to be precursors for the prebiotic synthesis of simple amino acids, which is thought to be important for understanding prebiotic chemistry (Calcutt et al. 2018).

Cyanoacetylene ( $\text{HC}_3\text{N}$ ), which is the shortest cyanopolyynne molecule, normally exists in warm and active star-forming regions (e.g. Yu et al. 2019; Feng et al. 2021). The University of Manchester Institute of Science and Technology (UMIST) database for astrochemistry<sup>2</sup> suggests that  $\text{HC}_3\text{N}$  has four main formation pathways, including the neutral–neutral reaction between  $\text{C}_2\text{H}_2$  and CN, the neutral–neutral reaction between  $\text{C}_2\text{H}$  and HNC, the ion–molecule reaction between  $\text{C}_3\text{H}_n^+$  ( $n = 3-5$ ) and nitrogen atoms, and the ion–molecule reaction between  $\text{C}_2\text{H}_2^+$  and HCN (McElroy et al. 2013). Up to now, it is not clear which formation pathway is the dominant one. Some theoretical models suggest that  $\text{C}_2\text{H}_2$  is released from the grain mantle and produces  $\text{HC}_3\text{N}$  by the neutral–neutral reaction between  $\text{C}_2\text{H}_2$  and CN (Hassel et al. 2008; Chapman et al. 2009; Taniguchi et al. 2019a). Using the isotopic fractionation method (e.g. Takano et al. 1998; Sakai et al. 2007), the neutral–neutral reaction between  $\text{C}_2\text{H}_2$  and CN was found to be the dominant formation pathway of  $\text{HC}_3\text{N}$  (e.g. Takano et al. 1998; Araki et al. 2016; Taniguchi et al. 2016). A number of chemical models (Taniguchi et al. 2019a) suggested that there is enhancement of the key reactions of cyanopolyynne formation upon sublimation of  $\text{CH}_4$  and  $\text{C}_2\text{H}_2$  from dust grains. As shocks heat and compress the surrounding gas, thereby releasing molecules (such as  $\text{CH}_4$  and  $\text{C}_2\text{H}_2$ ) trapped in the dust mantles into the gas phase (e.g. Arce et al. 2008), the released  $\text{CH}_4$  and  $\text{C}_2\text{H}_2$  would produce  $\text{HC}_3\text{N}$  in the gas phase. Therefore, shocks may be associated with the formation process of  $\text{HC}_3\text{N}$ . Investigation of the correlation between  $\text{HC}_3\text{N}$  and shock tracers may therefore help us to constrain the formation pathway of  $\text{HC}_3\text{N}$ .

Unsaturated interstellar complex organic molecules (iCOMs, e.g. Herbst & van Dishoeck 2009; Ceccarelli et al. 2017)<sup>3</sup>, such as  $\text{HC}_5\text{N}$  and  $\text{HC}_7\text{N}$ , are generally abundant in quiescent infrared dark clouds (quiescent) (Suzuki et al. 1992; Hirota et al. 2009). During the earliest phases of the star formation process, unsaturated iCOMs become deficient and saturated iCOMs (such as  $\text{CH}_3\text{OH}$  and  $\text{CH}_3\text{CN}$ ) become abundant instead in more evolved sources (e.g. Garrod & Herbst 2006; Herbst & van Dishoeck 2009). Such chemistry is known as ‘hot corino’ chemistry in low-mass star-forming regions (LMSFRs) and ‘hot core’ chemistry in high-mass star-forming regions (HMSFRs). However, various unsaturated iCOMs (e.g.  $\text{C}_4\text{H}_2$  and  $\text{HC}_5\text{N}$ ) have been detected in many LMSFRs (Sakai et al. 2008, 2009; Graninger et al. 2016; Law et al. 2018; Zhang et al. 2021). The theory of warm carbon-chain chemistry (WCCC) has been proposed, which is based on the gas-grain model (Sakai et al. 2009), and can explain the formation of cyanopolyyynes in LMSFRs with a formed protostar. As compared to the hot corino chemistry, in WCCC, unsaturated iCOMs can be formed in the gas phase when  $\text{CH}_4$  evaporates from grain mantle (Aikawa et al. 2008; Hassel et al. 2008) and are even more abundant in warm regions (20–30 K, Sakai et al. 2010).

The fact that unsaturated iCOMs can form in LMSFRs with a formed protostar naturally poses the question of whether un-

saturated iCOMs can also form in HMSFRs in advanced evolutionary stages. There have been a few successful observations of unsaturated iCOMs towards HMSFRs with a formed protostar (Esplugues et al. 2013; Belloche et al. 2013; Green et al. 2014; Feng et al. 2015; Taniguchi et al. 2018c). However, the sample with detection of unsaturated iCOMs (especially  $\text{HC}_7\text{N}$ ) is still small. Several models involving chemical networks suggest that unsaturated iCOMs could be formed in HMSFRs with a formed protostar (e.g. Chapman et al. 2009; Taniguchi et al. 2019a). These theoretical results were obtained by simulating certain sources (e.g. G305.2+0.2 in Chapman et al. 2009 and G28.28-0.36 in Taniguchi et al. 2019a) characterised by their specific properties. Therefore, unlike LMSFRs, there is no sufficient understanding of the formation of unsaturated iCOMs in HMSFRs with a formed protostar. Hence, more studies of unsaturated iCOMs in HMSFRs are required in order to obtain more details of their primary formation path.

We performed a cyanopolyyynes line survey in Ku band using the Shanghai Tian Ma 65m Radio Telescope (TMRT) to investigate the evolution of  $\text{HC}_3\text{N}$  in HMSFRs and the existence of  $\text{HC}_5\text{N}$  and  $\text{HC}_7\text{N}$  in HMSFRs with a formed protostar. In Sect. 2, we introduce our methods of sample selection and observations. We summarise our observational results and method of analysis in Sect. 3. We discuss the evolution of  $\text{HC}_3\text{N}$  in HMSFRs in Sect. 4.1. In Sect. 4.2, the relation between  $\text{HC}_3\text{N}$  and shock-tracing molecules ( $\text{H}_2\text{CO}$  and  $\text{SiO}$ ) is studied. In Sect. 4.3, we discuss unsaturated iCOMs in HMSFRs with a formed protostar. A short summary is presented in Sect. 5.

## 2. Sample selection and observations

### 2.1. Sample selection and distance

Successful surveys of unsaturated iCOMs ( $\text{HC}_5\text{N}$ ,  $\text{HC}_7\text{N}$  and  $\text{HC}_9\text{N}$  etc., Li et al. 2016; Zhang et al. 2017) in the C and Ku band were performed using TMRT. A systematic survey in C-band using TMRT was performed recently on a galactic radio recombination line (RRL) and a 6.7 GHz methanol maser towards a sample of 3348 sources obtained from the all-sky Wide-field Infrared Survey Explorer (WISE) point-source catalogue, applying colour criteria (Yang et al. 2017, 2019; Chen et al. 2020). The 6.7 GHz  $\text{CH}_3\text{OH}$  maser and RRL were detected in 240 sources and 517 sources, respectively. A HMSFRs sample consisting of 654 sources was built by consolidating the 6.7 GHz  $\text{CH}_3\text{OH}$  maser sample and the RRL sample (Chen et al. 2020). This incorporates three subsamples of sources, namely 137 sources with detection of the 6.7 GHz  $\text{CH}_3\text{OH}$  maser alone (hereafter Maser-only), 414 sources with detection of the RRL alone (RRL-only), and 103 sources with detection of both (Maser-RRL). It was suggested that these three types of sources correspond to different star-forming stages, taking into consideration that the methanol maser should appear before the formation of the HII region (Chen et al. 2020).

The sources with the strong 6.7 GHz  $\text{CH}_3\text{OH}$  maser (flux density  $>0.4$  Jy) or RRL emission ( $T_{\text{peak}} > 0.02$  K) that also have a galactocentric distance distribution (ranging from 3 to 12 kpc) similar to that of the original HMSFRs sample (3–13 kpc, Chen et al. 2020) were chosen as our targets in order to improve the detection rate of cyanopolyyynes. We then chose 50 targets from each class.

The selected sources have accurate heliocentric distances, which were determined from trigonometric parallax measurements (Reid et al. 2014, 2019) or the latest parallax-based dis-

<sup>2</sup> <http://udfa.ajmarkwick.net/>

<sup>3</sup> Unsaturated iCOMs are carbon-bearing molecules that have at least six atoms and are hydrogen poor (e.g. Rolffs et al. 2011; Rathborne et al. 2011)

tance calculator V2<sup>4</sup>. The galactocentric distances of our sources were then determined using the heliocentric distance according to the following formula (Roman-Duval et al. 2009):

$$D_{\text{GC}} = \sqrt{[R_0 \cos(l) - D \cos(b)]^2 + R_0^2 \sin^2(l)}, \quad (1)$$

where  $R_0$  is the galactocentric distance of the sun, which is equal to  $8.122 \pm 0.031$  kpc (Gravity Collaboration et al. 2018),  $l$  and  $b$  are the Galactic longitude and Galactic latitude, respectively, and  $D$  is the heliocentric distance (Table B.1).

## 2.2. Observations

We carried out a cyanopolyyne line survey in August, September, and October 2018, April, May, November, and December 2019, and January 2020 using the 65m TMRT located in Shanghai, China. Due to limited observation time, we observed 123 sources comprising 29 Maser-only, 50 Maser-RRL, and 44 RRL-only ones, while the remaining 27 sources, which are relatively weak, were not observed. In view of our detection rate, several detections among these 27 relatively weak sources could be missed. However, this should not introduce significant error in our results. Using a cryogenically cooled Ku band receiver with the frequency coverage of 12-18 GHz and the DIBAS (Digital Backend System) being a Field-Programmable Gate Array (FPGA)-based spectrometer (Bussa 2012), we were able to receive and record the signals. Mode 22, which has 16 spectral windows, was used in our observations. Each window has 16384 channels with bandwidths of 23.4375 MHz and a frequency resolution of 1.431 kHz. The centre frequency setups for our observations of cyanopolyynes are listed in Table 1. The half power beam widths (HPBWs) of TMRT at the transitions of  $\text{HC}_3\text{N}$  ( $J = 2-1$ ),  $\text{HC}_5\text{N}$  ( $J = 6-5$ ), and  $\text{HC}_7\text{N}$  ( $J = 15-14$ ) were about  $52''$  at 18195.31 MHz,  $60''$  at 15975.93 MHz, and  $56''$  at 16919.98 MHz, respectively. The typical root mean square (rms) was about 10 mK. The original velocity resolution was  $0.02 \text{ km s}^{-1}$  for  $\text{HC}_3\text{N}$  ( $J = 2-1$ ), and  $0.03 \text{ km s}^{-1}$  for  $\text{HC}_5\text{N}$  ( $J = 6-5$ ) and  $\text{HC}_7\text{N}$  ( $J = 15-14$ ). The system temperatures were about 30-80 K in the Ku band. A noise diode was used for calibration. The uncertainty on the antenna temperature ( $T_A^*$ ) was about 20%. The main beam brightness temperature ( $T_{\text{mb}}$ ) was obtained from the antenna temperature as  $T_{\text{mb}} = T_A^*/\eta_{\text{mb}}$ , where the main beam efficiency ( $\eta_{\text{mb}}$ ) of the TMRT was about 0.6 in the Ku band (Wang et al. 2017). During our observations, we adopted a position-switching mode with the off-position at  $(-30', 0)$  or  $(30', 0)$  offset in azimuth and elevation from the source. Each cycle adopted 2 mins for both ON position and OFF position and each source was observed for 15 ON-OFF cycles. For a few weak objects, more scans were adopted to improve the signal-to-noise ratio (S/N) of the molecular lines.

## 3. Results and analyses

The GILDAS/CLASS<sup>5</sup> software was used for the data reduction. Poor scans (system temperature  $>80$  K) were removed and the rest of the scans were averaged to improve the S/N. Linear or multi-order ( $<4$ ) polynomial baselines were subtracted for the spectra. To further improve the S/N, the spectra were smoothed with a velocity resolution of  $\sim 0.4 \text{ km s}^{-1}$ . Among six hyperfine structure (HFS) lines of  $\text{HC}_3\text{N}$  ( $J = 2-1$ ) (e.g. Levshakov et al.

2010; Li et al. 2016), only blended lines of the  $J = 2-1$ ,  $F = 3-2$  and  $J = 2-1$ ,  $F = 2-1$  transitions were detected towards our targets, except for G30.810-0.050. In this latter source, two extra groups of HFS components, that is,  $F=1-1$ , and unresolved  $F=2-2$  and  $F=1-0$  were also detected. Due to the presence of the spectra with unresolved HFS components, the Gaussian method was used to fit the spectra instead of the HFS fitting method.

We successfully detected the  $\text{HC}_3\text{N}$  ( $J = 2-1$ ) emission line in 38 HMSFRs ( $S/N > 3$ ) towards 123 sources, which results in a detection rate of 31%. The sources with  $\text{HC}_3\text{N}$  detection include 10 Maser-only, 22 Maser-RRL, and 6 RRL-only sources with detection rates of 34%, 44%, and 14%, respectively. As far as we know, among our 38  $\text{HC}_3\text{N}$  ( $J = 2-1$ ) sources, 34 are newly detected (except G24.328+0.144, G24.790+0.084, G49.466-0.408 and G111.532+0.759, Widicus Weaver et al. 2017). Among the 38 sources with  $\text{HC}_3\text{N}$  detection, the  $\text{HC}_5\text{N}$  ( $J = 6-5$ ) line was also detected in 11 sources with a detection rate of  $\sim 29\%$ , including 2 Maser-only and 9 Maser-RRL sources with the detection rates of  $\sim 20\%$  and  $\sim 41\%$ , respectively. Apart from G24.790+0.084 (Green et al. 2014), another 10 sources were new  $\text{HC}_5\text{N}$  detections. The  $\text{HC}_7\text{N}$  ( $J = 15-14$ ) transition was first detected in G24.790+0.084. All spectra for  $\text{HC}_3\text{N}$ ,  $\text{HC}_5\text{N}$ , and  $\text{HC}_7\text{N}$  are shown in Fig. 1, where solid and dashed lines show the local standard of rest (LSR) velocities of 6.7 GHz  $\text{CH}_3\text{OH}$  maser (Yang et al. 2017, 2019) and RRL (Chen et al. 2020), respectively. The small differences in LSR velocity for these three molecules may be due to the fact that the molecules have different excitation mechanisms and exist in HMSFRs with different characteristics. The spectral line parameters of  $\text{HC}_3\text{N}$  and unsaturated iCOMs ( $\text{HC}_5\text{N}$  and  $\text{HC}_7\text{N}$ ) are listed in Tables B.1 and B.2, respectively.

### 3.1. Column density of cyanopolyynes

The  $\text{HC}_3\text{N}$  ( $J = 2-1$ ) line is generally considered to be optically thin (e.g. McGee et al. 1975; Gong et al. 2015; Li et al. 2016). Among our detected sources, the strongest, G30.810-0.050, was found to have three groups of HFS structure components of  $\text{HC}_3\text{N}$  ( $J = 2-1$ ). We can determine the optical depth of its  $\text{HC}_3\text{N}$  ( $J = 2-1$ ) line using the HFS fitting method implemented in CLASS software ('Method' command) as shown in Fig. 2. A low optical depth value of  $<0.1$  is obtained, which supports the idea that the optical depth effect is insignificant and cannot be used for further analysis.

The volume density of  $\text{H}_2$  can be estimated as  $n_{\text{H}_2} = N_{\text{H}_2}/(2DR_{\text{eff}})$  (Urquhart et al. 2014a; König et al. 2017), where  $N_{\text{H}_2}$  and  $R_{\text{eff}}$  are the column density of  $\text{H}_2$  and the effective radius of the clump in rad (Table 2), respectively, and  $D$  is the heliocentric distance (Table B.1). The lowest value of the volume density for our sources is about  $2.1 \times 10^3 \text{ cm}^{-3}$  (G24.328+0.144), which is larger than the critical density<sup>6</sup> of  $\text{HC}_3\text{N}$  ( $J = 2-1$ ) ( $n_{\text{crit}} = 9.7 \times 10^2 \text{ cm}^{-3}$ , with a kinetic temperature of 10 K, Shirley 2015). This suggests that the  $\text{HC}_3\text{N}$  molecule is under local thermodynamic equilibrium (LTE).  $\text{HC}_5\text{N}$  and  $\text{HC}_7\text{N}$  are generally assumed to be in LTE as well (e.g. Li et al. 2016; Taniguchi et al. 2018a; Wu et al. 2019; Zhang et al. 2021). Therefore, assuming LTE conditions and a negligible optical depth value, the column density can be estimated by the follow-

<sup>6</sup> The critical density is estimated from  $n_{\text{crit}} = A_{ij}/C_{ij}$  for optically thin emission, where  $A_{ij}$  and  $C_{ij}$  is the Einstein coefficient for spontaneous emission and the collision rate, respectively (Shirley 2015).

<sup>4</sup> <http://bessel.vlbi-astrometry.org/node/378>

<sup>5</sup> <https://www.iram.fr/IRAMFR/GILDAS/>

ing equation(Cummins et al. 1986):

$$N = \frac{3k_B W}{8\pi^3 \nu S \mu^2} Q(T_{\text{rot}}) \frac{T_{\text{rot}}}{T_{\text{rot}} - T_{\text{bg}}} \exp(E_u/k_B T_{\text{rot}}), \quad (2)$$

where  $k_B$  is the Boltzmann constant,  $W$  is the integrated line intensity,  $\nu$  is the rest frequency of the transition, and  $T_{\text{rot}}$  and  $T_{\text{bg}}$  are the rotational temperature and the background temperature (2.73 K), respectively. Also,  $E_u/k_B$  and  $S\mu^2$  (taken from Cologne Database for Molecular Spectroscopy, CDMS<sup>7</sup>) are the upper level energy in K and the product of the line strength and the square of the electric dipole moment, respectively (see Table 1). The partition functions,  $Q(T_{\text{rot}})$ , of each molecule are taken from CDMS:

$$Q(\text{HC}_3\text{N}) = 4.582 T_{\text{rot}} + 0.283 \quad (3)$$

$$Q(\text{HC}_5\text{N}) = 7.595 \times 10^{-7} T_{\text{rot}}^4 - 3.760 \times 10^{-4} T_{\text{rot}}^3 + 5.177 \times 10^{-2} T_{\text{rot}}^2 + 13.38 T_{\text{rot}} + 23.15 \quad (4)$$

$$Q(\text{HC}_7\text{N}) = 1.633 \times 10^{-6} T_{\text{rot}}^4 - 7.706 \times 10^{-4} T_{\text{rot}}^3 - 9.174 \times 10^{-2} T_{\text{rot}}^2 + 119 T_{\text{rot}} - 96.46. \quad (5)$$

For molecular transitions under LTE conditions, the rotation temperature is usually determined by the rotation diagram method (e.g. Goldsmith & Langer 1999). Application of this method requires at least two transition lines of each molecule to be available. However, our observations provide only one transition line for each molecule.

Here,  $T_{\text{rot}}$  was taken from the rotational temperature of  $\text{NH}_3$ , which could be obtained from the  $\text{NH}_3$  inversion lines and was widely used as a good tracer of temperature in the molecular clouds (Tafalla et al. 2004; Mangum & Shirley 2015; Wang et al. 2020). Notably,  $\text{NH}_3$  and cyanopolyyynes may come from different regions in the clumps and therefore lead to error in calculations of the column density of cyanopolyyynes. However,  $\text{HC}_3\text{N}$  and  $\text{NH}_3$  have similar critical densities, when the kinetic temperature is in the range of 10 to 50 K (Shirley 2015). Therefore, the use of  $T_{\text{rot}}$  of  $\text{NH}_3$  should not cause any significant bias in our calculations of the column density of cyanopolyyynes. The rotational temperature of  $\text{NH}_3$  was reported in 23 sources among the total of 38 sources with  $\text{HC}_3\text{N}$  detection (Wienen et al. 2012; Urquhart et al. 2011; Li et al. 2016; Chira et al. 2013). For another 6 sources (G20.234+0.085, G24.328+0.144, G24.528+0.337, G24.790+0.084, G28.287-0.348, and G192.600-0.048), only the optical depth ( $\tau$ ) and the main beam temperatures ( $T_{\text{mb}}$ ) of  $\text{NH}_3$  lines were reported (Cyanowski et al. 2013; Svoboda et al. 2016; Yang et al. in prep.). For these sources,  $T_{\text{rot}}$  of  $\text{NH}_3$  was derived as follows (e.g. Ragan et al. 2011):

$$T_{\text{rot}} = -41.5 \left[ \ln\left(\frac{-0.283}{\tau(1, 1, m)}\right) \ln\left[1 - \frac{T_{\text{mb}}(2, 2, m)}{T_{\text{mb}}(1, 1, m)}(1 - e^{-\tau(1, 1, m)})\right] \right]^{-1}, \quad (6)$$

where  $m$  represents the main hyperfine component. Therefore, we obtained the  $T_{\text{rot}}$  values of  $\text{NH}_3$  for 29 sources from our sample with  $\text{HC}_3\text{N}$  detection, including 9 Maser-only, 19 Maser-RRL, and 1 RRL-only sources. For 9 sources without  $T_{\text{rot}}$  (1 Maser-only, 3 Maser-RRL, and 5 RRL-only), the average  $T_{\text{rot}}$  value of each type was used as their  $T_{\text{rot}}$  values (Table B.3). The column densities of cyanopolyyynes molecules were obtained using the values of  $T_{\text{rot}}$  of  $\text{NH}_3$  and Eq. (2) (Table B.3).

We made a comparison with the published  $\text{HC}_3\text{N}$  column densities towards our sample. These were found to be  $2.00 \times 10^{13} \text{ cm}^{-2}$  for G28.287-0.348 (Taniguchi et al. 2018b) and  $3.60 \times 10^{13} \text{ cm}^{-2}$  for G81.752-0.691 (DR21, Chung et al. 1991), which are comparable to our results ( $1.10 \times 10^{13} \text{ cm}^{-2}$  for G28.287-0.348 and  $3.12 \times 10^{13} \text{ cm}^{-2}$  for G81.752-0.691, respectively). The mean column density of  $\text{HC}_3\text{N}$  was found to be  $(1.75 \pm 0.42) \times 10^{13} \text{ cm}^{-2}$  for Maser-only,  $(2.84 \pm 0.47) \times 10^{13} \text{ cm}^{-2}$  for Maser-RRL, and  $(0.82 \pm 0.15) \times 10^{13} \text{ cm}^{-2}$  for RRL-only sources. More details about the differences in the column density between these three types of sources is discussed in Sect. 4.1.

### 3.2. Far-infrared spectral energy distributions

The Herschel infrared Galactic Plane Survey (Hi-GAL, Molinari et al. 2016) compact-source catalogue was obtained by performing photometry of Herschel images (70, 160, 250, 350 and 500  $\mu\text{m}$ ). Urquhart et al. (2014a) conducted a photometry of the Atacama Pathfinder Experiment (APEX, Güsten et al. 2006) images (870  $\mu\text{m}$ ) with the source-extraction routine SExtractor<sup>8</sup> and obtained the APEX Telescope Large Area Survey of the Galaxy (ATLASGAL, Schuller et al. 2009; Contreras et al. 2013) compact-source catalogue. Using a search radius of 30" (roughly half the HPBW of the  $\text{HC}_3\text{N}$ ), we cross-identified both catalogues with our  $\text{HC}_3\text{N}$  sources. Twenty-one sources were found in both catalogues and their IR flux data are presented in Table 2. In a number of previous works (e.g. Wu et al. 2019; Elia et al. 2010), a single-temperature grey-body model was used to fit the spectral energy distributions (SEDs) of these sources. The Levenberg-Marquardt algorithm provided in the Python package lmfit was applied (Newville et al. 2016). The grey-body model can be expressed as follows:

$$S_\nu = \frac{M \kappa_0}{D^2 \gamma} \left(\frac{\nu}{\nu_0}\right)^\beta B_\nu(T_d), \quad (7)$$

where  $M$  is the total (dust + gas) mass,  $\kappa_0 = 1.85 \text{ cm}^2 \text{ g}^{-1}$  is the dust opacity at 870  $\mu\text{m}$  (Ossenkopf & Henning 1994),  $B_\nu(T_d)$  is the Planck function at the dust temperature  $T_d$ ,  $\beta$  is the dust emissivity index (the mean value of 1.75 was used for all dust models, Ossenkopf & Henning (1994)), and  $\gamma$  is the gas-to-dust ratio, which depends on the galactocentric distance of the source (Giannetti et al. 2017):

$$\gamma = 10^{0.087 \times D_{\text{GC}} + 1.44}. \quad (8)$$

The derived values of  $\gamma$  are listed in Table 2. Figure 3 shows the fitting results of the far-infrared (FIR) SEDs of our sources. Similar to the previous works, the Herschel 70  $\mu\text{m}$  data were excluded in our grey-body fitting because of their origin from a warm dust component and a large fraction of this emission coming from very small grains (e.g. Wu et al. 2019; Guzmán et al. 2015). The dust temperature  $T_d$  and the total mass  $M$  were obtained from the SED fit, and are presented in Table 2. For comparison, we collected the results of  $T_d$  and  $M$  of our 21 sources (listed in Table 2), which were derived in ATLASGAL (Urquhart et al. 2018). There are eight sources with  $M$  values consistent with those of Urquhart et al. (2018) within the error range, while all the others show a large difference in  $M$  values between ours and theirs. The values of  $T_d$  for our sources are smaller than those of Urquhart et al. (2018). The difference should be mainly caused by the different fitting models used, that is, a two-component (grey-body and black-body) model was used by these latter authors, while we used a single component model.

<sup>7</sup> <https://cdms.astro.uni-koeln.de/cdms/portal/>

<sup>8</sup> <https://sextractor.readthedocs.io/en/latest/License.html>

### 3.3. Relative abundance of cyanopolyyne to $H_2$

To obtain the relative abundance of cyanopolyyne with respect to  $H_2$  for our sources, we first estimated  $N_{H_2}$  in these sources. Under the assumption of optically thin dust emission at 870  $\mu m$ , the beam-averaged  $H_2$  column density can be calculated using the following expression Schuller et al. (2009):

$$N_{H_2} = \frac{F_{870\gamma}}{B_{870}(T_d)\Omega_{app}\kappa_0\mu_{H_2}m_H}, \quad (9)$$

where  $F_{870}$  is the peak flux density (see Table 2) and  $\Omega_{app}$  is the beam solid angle. For a source located at  $D$ ,  $\Omega_{app} = A/D^2$ , where  $A = R_{eff}^2\pi$  is the surface area of the source. The value of  $R_{eff}$  is presented in Table 2. Here,  $m_H$  is the mass of a hydrogen atom, and  $\mu_{H_2} = 2.8$  is the mean molecular weight per  $H_2$  molecule (Kauffmann et al. 2008).  $B_{870}(T_d)$  is the intensity of the black-body at 870  $\mu m$  at the dust temperature  $T_d$ , which was determined from the SED fit (Sect. 3.2). We obtained the column densities of  $H_2$  for 21 sources, including 6 Maser-only, 13 Maser-RRL, and 2 RRL-only sources (Table 2).

Using the results of the column density of cyanopolyyne (Table B.3) and  $H_2$  (Table 2), we derived the relative abundances of cyanopolyyne with respect to  $H_2$  ( $X(a) = N(a)/N_{H_2}$  —where  $a$  refers to cyanopolyyne—for 21 sources (Table B.3). The mean relative abundance of  $HC_3N$  was found to be  $(1.22 \pm 0.52) \times 10^{-10}$  for Maser-only sources,  $(5.40 \pm 1.45) \times 10^{-10}$  for Maser-RRL sources, and  $(1.65 \pm 1.50) \times 10^{-10}$  for RRL-only sources. In Sect. 4.1, we discuss the differences in relative abundance between our three types of sources.

## 4. Discussion

### 4.1. Evolution of $HC_3N$

The definitions of the evolutionary stages of HMSFRs, including physical and chemical classifications, are still not clear (Hoq et al. 2013; Miettinen 2014; Gerner et al. 2014; Urquhart et al. 2014b; Zhang et al. 2016; König et al. 2017; Urquhart et al. 2019, 2022). Based on the physical properties of the clumps, the sequence of a HMSFR is usually divided into four evolutionary stages: quiescent, high-mass protostellar object (protostellar), massive young stellar object (YSO), and  $H\alpha$  region (see Urquhart et al. 2019, 2022, and references therein).

Urquhart et al. (2019) carried out a 3mm molecular-line survey towards a large sample consisting of 570 high-mass star-forming clumps and found a trend in the detection rate of  $HC_3N$  ( $J = 10-9$ ), namely an increase from quiescent, to protostellar, to YSO, and then a slight decrease in  $H\alpha$  region (including all  $H\alpha$  region stages). Yu et al. (2019) subdivided  $H\alpha$  regions into ultra-compact (UC)  $H\alpha$  regions and normal classical  $H\alpha$  regions. By analysing the archival available data from the Hi-GAL and the Millimetre Astronomy Legacy Team Survey at 90 GHz (MALT90)<sup>9</sup>, these latter authors found that the abundance of  $HC_3N$  could increase in UC  $H\alpha$  regions, while it decreases or reaches a plateau in normal classical  $H\alpha$  regions.

The results of our analysis (Sect. 3) show that the detection rates of  $HC_3N$  are 34%, 44%, and 14% for Maser-only, Maser-RRL, and RRL-only sources, respectively. The mean column density of  $HC_3N$  is found to be  $(1.75 \pm 0.42) \times 10^{13} \text{ cm}^{-2}$  for Maser-only sources,  $(2.84 \pm 0.47) \times 10^{13} \text{ cm}^{-2}$  for Maser-RRL sources, and  $(0.82 \pm 0.15) \times 10^{13} \text{ cm}^{-2}$  for RRL-only sources. The average values of the relative abundance of  $HC_3N$  are

$(1.22 \pm 0.52) \times 10^{-10}$ ,  $(5.40 \pm 1.45) \times 10^{-10}$ , and  $(1.65 \pm 1.50) \times 10^{-10}$  for Maser-only, Maser-RRL, and RRL-only sources, respectively. Those results are plotted as a function of source classification in Fig. 4. All the results show the same trend, namely an increase from Maser-only to Maser-RRL sources and a decrease from Maser-RRL to RRL-only ones.

The 6.7 GHz  $CH_3OH$  maser is excited according to the infrared radiative pumping mechanism in the disc when a formed protostar begins to warm its natal environment. This is normally considered to be related to the early stages of HMSFRs when there is significant mass accretion (e.g. Sobolev & Deguchi 1994; Minier et al. 2003; Ellingsen 2006; Xu et al. 2008). Based on the  $CH_3OH$  maser line and radio continuum mapping observations towards a sample of HMSFRs, Walsh et al. (1998) found that the 6.7 GHz  $CH_3OH$  maser is observable before the UC  $H\alpha$  regions (YSOs) and are probably destroyed as the UC  $H\alpha$  regions develop. Therefore, we assume our Maser-only sources in YSOs.

Based on the statistical investigations towards different types of masers, Ellingsen (2007) and Breen et al. (2010) proposed an evolutionary sequence for masers in HMSFRs and suggested that 6.7 GHz  $CH_3OH$  maser can exist in UC  $H\alpha$  regions, although most of them are located at earlier YSO stages. Considering this, as well as the fact that RRL appears after the formation of the  $H\alpha$  region, we propose that our Maser-RRL sources are found in the more evolved UC  $H\alpha$  regions.

RRL are produced by scattering of free electrons off the ions, which come from the surrounding  $H\alpha$  gas ionised by high-energy ultraviolet (UV) photons ( $> 13.6 \text{ eV}$ ) from formed massive stars. RRL is a powerful tool to track  $H\alpha$  regions (Walsh et al. 1998; Bernasconi & Maeder 1996; Anderson et al. 2011, 2014, 2018; Condon & Ransom 2016; Luisi et al. 2018; Zhang et al. 2022). As RRLs are undetectable in young dense UC  $H\alpha$  regions and at their previous stages due to the effect of beam dilution and high optical depth (e.g. Churchwell 2002; Chen et al. 2020), our RRL-only sources should belong to more extended and evolved normal classical  $H\alpha$  regions.

Based on these assumptions, our results concerning Maser-only sources (YSO, 34%), which have a relatively high detection rate for  $HC_3N$  compared to Maser-RRL and RRL-only sources ( $H\alpha$  region,  $\sim 30\%$ ), are identical to those of Urquhart et al. (2019). Our results concerning Maser-RRL, namely with the largest abundance of  $HC_3N$  at this stage and a decrease from Maser-RRL (UC  $H\alpha$  region) to RRL-only (normal classical  $H\alpha$  region) sources, are consistent with those of Yu et al. (2019), that is a decrease from UC  $H\alpha$  to normal classical  $H\alpha$  regions. The UMIST database for astrochemistry suggested that  $HC_3N$  molecules could be destroyed by a reaction with a UV photon, which produces CN and CCH or  $HC_3N^+$  and an electron (McElroy et al. 2013). Therefore, the decrease in  $N(HC_3N)$  between UC  $H\alpha$  regions and normal classical  $H\alpha$  regions may reflect the possibility of a destruction of  $HC_3N$  by UV photons, which is consistent with the observations of Yu & Xu (2016). The increase in the column density of  $HC_3N$  between YSOs and UC  $H\alpha$  regions is likely correlated with the increase in dust temperature, which results in a more desorbed progenitor (e.g.  $C_2H_2$ ,  $CH_4$ ) of  $HC_3N$  from the dust grain and a further increase in the amount of  $HC_3N$  by gas phase reactions (Yu et al. 2019; Taniguchi et al. 2019b).

However, this evolutionary picture needs to be confirmed by comparing the physical parameters (such as luminosity, mass, and  $T_{dust}$ ) of these three types of samples, as in Molinari et al. (2008). This issue will be discussed in a forthcoming paper (Chen et al. In prep.; private communication).

<sup>9</sup> <http://atoa.atnf.csiro.au/MALT90>

## 4.2. $\text{HC}_3\text{N}$ : another tracer of shock?

Based on its spectra with large line-width and wing emissions (Beltrán et al. 2004; Yu & Wang 2015; Taniguchi et al. 2018c; Yu et al. 2019; Feng et al. 2021), and some theoretical modelling works on L1157-B1 (Viti et al. 2011; Benedettini et al. 2013; Mendoza et al. 2018),  $\text{HC}_3\text{N}$  was proposed to be a species originating from outflow shock within active star-forming regions. Here, by analysing the relation between  $\text{HC}_3\text{N}$  and other shock tracers, we study whether or not  $\text{HC}_3\text{N}$  is a good tracer of shock.

Towards our  $\text{HC}_3\text{N}$  sample, we collected the  $\text{H}_2\text{CO}$  line intensity data from the TMRT C band survey (private communication, Dr. X. Chen). Using these data, we further calculated the column density of  $\text{H}_2\text{CO}$  of our sample, as for cyanopolyyynes in sample Sect. 3.1. Our column density results for  $\text{H}_2\text{CO}$  are presented in Table B.4. The derived column densities range from  $0.45$  to  $61.49 \times 10^{13} \text{ cm}^{-2}$ , the mean value being equal to  $(7.78 \pm 3.25) \times 10^{13} \text{ cm}^{-2}$ . Our results are consistent with values calculated from previous observations towards one ATLASGAL HMSFR sample, which range from  $0.48$  to  $61 \times 10^{13} \text{ cm}^{-2}$ , the mean value being  $(7.8 \pm 1.3) \times 10^{13} \text{ cm}^{-2}$ , and the predictions of the RADEX non-LTE model (Tang et al. 2018).

Figure 5 (upper left panel) presents the column density of  $\text{H}_2\text{CO}$  versus that of  $\text{HC}_3\text{N}$  for our sample. A correlation between these characteristics can be seen, albeit with large scatter; that is,  $N_{\text{HC}_3\text{N}}$  tends to be stronger in the sources with larger  $N_{\text{H}_2\text{CO}}$ . A weighted least-squared linear fit gives  $N_{\text{HC}_3\text{N}} = (0.28 \pm 0.06) \times N_{\text{H}_2\text{CO}} + (0.92 \pm 0.28)$ , with a correlation coefficient of 0.77, and the errors representing  $1\sigma$  standard deviations. A similar correlation can also be found between the line intensities (with a Pearson correlation of 0.57, upper right panel), which reflects non-significant Malmquist bias on the correlation of their column densities.

For another shock tracer,  $\text{SiO}$ , we collected the data for our sample, including the integrated line intensity and the corresponding column density (Csengeri et al. 2016). In Fig. 5, we plotted the column density (bottom left panel) and the integrated line intensity (bottom right panel) of  $\text{HC}_3\text{N}$  versus those for  $\text{SiO}$  for our sample. Both panels show a significant correlation between  $\text{SiO}$  and  $\text{HC}_3\text{N}$ , which reflects no significant selection bias. For the column density, a weighted least-squares linear fit (solid line) gives  $N_{\text{HC}_3\text{N}} = (1.63 \pm 0.22) \times N_{\text{SiO}} + (0.85 \pm 0.26)$ , with a larger correlation coefficient of 0.94 than that found for  $\text{H}_2\text{CO}$  and  $\text{HC}_3\text{N}$ .

Similar strong correlations between the parameters for  $\text{HC}_3\text{N}$  and  $\text{SiO}$  were also found before based on the results for a sample of 43 southern HMSFRs. These parameters included the line width, the integrated line intensity, the column density, and the relative abundance (He et al. 2021). For comparison, the column density results (empty circles) with the weighted least-squares linear fitting line (the dashed line) are also shown in Fig. 5 (bottom left panel). The strong correlation between  $\text{HC}_3\text{N}$  and  $\text{SiO}$  is consistent, although their column densities cover larger ranges and their fit line has a larger slope. Both results in the literature and ours suggest a strong correlation between  $\text{HC}_3\text{N}$  and  $\text{SiO}$  in terms of integrated line intensity and column density.

Taking  $\text{H}_2\text{CO}$  and  $\text{SiO}$  molecules as good tracers of shock, positive correlations between them and  $\text{HC}_3\text{N}$  support the idea of a shock origin of  $\text{HC}_3\text{N}$ . Under the impact of shocks,  $\text{C}_2\text{H}_2$ , being the precursor molecule of  $\text{HC}_3\text{N}$ , is released from dust grains to the gas phase and reacts with  $\text{CN}$  to form  $\text{HC}_3\text{N}$ . This is in agreement with the findings of Taniguchi et al. (2019a) from chemical models that the sublimation of  $\text{CH}_4$  and  $\text{C}_2\text{H}_2$  from dust grains enhances key reactions of the formation of

cyanopolyyynes. Therefore, our results indirectly suggest that the neutral-neutral reaction between  $\text{C}_2\text{H}_2$  and  $\text{CN}$  is the dominant formation pathway of  $\text{HC}_3\text{N}$ . In addition, shock models indicate that  $\text{HC}_3\text{N}$  abundance would be strongly enhanced as a consequence of the passage of the shock (Mendoza et al. 2018). The presence of a C-type shock with a pre-shock density  $> 10^4 \text{ cm}^{-3}$  and a velocity of  $\sim 40 \text{ km s}^{-1}$  (to reach the maximum shock temperature of 4000 K) can produce the observed high abundance of  $\text{HC}_3\text{N}$  (Benedettini et al. 2013). Meanwhile, silicon monoxide ( $\text{SiO}$ ) mainly originates from jets probing accretion processes (e.g. Codella et al. 1999; Duarte-Cabral et al. 2014; Cosentino et al. 2018). Under the action of high-velocity (20-50  $\text{km s}^{-1}$ ) shocks, Si atoms and Si-bearing molecules from the dust grains are evaporated to the gas phase and are subsequently oxidised to  $\text{SiO}$  (Martin-Pintado et al. 1992; Gusdorf et al. 2008; López-Sepulcre et al. 2016). However,  $\text{H}_2\text{CO}$  is formed on the surface of dust grains by consecutive hydrogenation of  $\text{CO}$ , which can be released to the gas phase by shocks with relatively low velocity ( $\sim 15 \text{ km s}^{-1}$ ) (Mitchell 1984; Codella et al. 2010; Tafalla et al. 2010). Therefore,  $\text{SiO}$  and  $\text{HC}_3\text{N}$  may trace similar high-velocity shock regions, while  $\text{H}_2\text{CO}$  traces relatively low-velocity shock ones. This is in agreement with our results, which show a stronger correlation between  $\text{SiO}$  and  $\text{HC}_3\text{N}$  than that seen between  $\text{H}_2\text{CO}$  and  $\text{HC}_3\text{N}$ .

To further confirm the dominant formation pathway of  $\text{HC}_3\text{N}$ , we can investigate the correlation between  $\text{C}_2\text{H}_2$  and  $\text{HC}_3\text{N}$  towards sources with shocks and carry out observations of  $\text{HC}_3\text{N}$  and its three isotopologues towards a large sample. Moreover, observations of the spatial distribution of different shock tracers are needed to find the similarities and differences in terms of their physical and chemical properties.

## 4.3. Unsaturated iCOMs in HMSFRs with a formed protostar

As mentioned in Sect. 1, unsaturated iCOMs were previously thought to be destroyed in 'hot core' chemistry. However, some observational and theoretical studies seem to indicate that  $\text{HC}_5\text{N}$  and even  $\text{HC}_7\text{N}$  can be present in the protostellar or hot molecule cores (HMCs, which are the sources around YSOs with a rich molecular line spectrum; Kurtz et al. 2000; Cesaroni 2005; Hosokawa & Omukai 2009; Rathborne et al. 2011; Liu et al. 2021). Unlike LMSFRs, the formation pathway of unsaturated iCOMs in HMSFRs with a formed protostar is not yet clear.

Our survey successfully detected  $\text{HC}_5\text{N}$   $J = 6-5$  transition ( $E_u/k_B \sim 2.68 \text{ K}$ ) in 11 sources (10 of them are new) among 123 targeted HMSFRs (Sect. 3). Combined with previous observations (Green et al. 2014; Taniguchi et al. 2018c),  $\text{HC}_5\text{N}$  was detected in 60 HMSFRs with a formed protostar. Furthermore, our first detection of the  $\text{HC}_7\text{N}$   $J = 15-14$  transition ( $E_u/k_B \sim 5.68 \text{ K}$ ) in G24.790+0.084 leads to three  $\text{HC}_7\text{N}$  sources in three HMSFRs with a formed protostar (Orion KL in Feng et al. 2015 and G28.28-0.36 in Taniguchi et al. 2018a). Our detections enlarge the  $\text{HC}_5\text{N}$  and  $\text{HC}_7\text{N}$  samples and confirm that unsaturated iCOMs can exist in YSOs and UC HII regions, which is consistent with the predictions of the chemical model of Chapman et al. (2009). However, our observations may be contaminated by the low-temperature gas without star-forming activity because of the large beam size ( $\sim 53''$ ) and low  $J$  transition with low level energy of molecular transitions ( $< 10 \text{ K}$ ). Therefore, follow-up observations of high  $J$  molecular transitions with high spatial resolution would help to confirm the origin of  $\text{HC}_5\text{N}$  and  $\text{HC}_7\text{N}$ . More modelling works on iCOM chemistry are also needed to improve our understanding of unsaturated iCOMs.

It is also interesting that we find a significant difference in the column density ratio  $HC_3N/HC_5N$  between our subsamples (Table B.3). The mean value of the ratio of  $10.45 \pm 2.89$  for Maser-RRL sources exceeds that of Maser-only sources of  $4.11 \pm 0.46$  by a factor of about three. However, the ratio of  $N(HC_3N)/N(HC_5N)$  seems to decrease with time as obtained from the simulation result (Taniguchi et al. 2019a). Further investigations on large samples and more targeted chemical simulations are required to check whether the  $N(HC_3N)/N(HC_5N)$  ratio can be used as a chemical clock, given that the relative abundances of different molecules changes with time (Wakelam et al. 2004).

## 5. Summary

We present a cyanopolyne ( $HC_{2n+1}N$ ) line survey in the Ku band (12–18 GHz) towards a large sample of 123 HMSFRs using the TMRT. The sample was divided into 29 sources with detection of the 6.7 GHz  $CH_3OH$  maser alone (Maser-only), 44 sources with detection of RRL alone (RRL-only), and 50 sources with both maser and RRL (Maser-RRL). Our main results can be summarised as follows:

1. Among 123 targets,  $HC_3N$  is detected in 38 sources (including 34 new ones), which include 10 Maser-only, 22 Maser-RRL, and 6 RRL-only sources. The detection rates are 34%, 44%, and 14% for Maser-only, Maser-RRL, and RRL-only sources, respectively.
2. The mean column densities of  $HC_3N$  are  $(1.75 \pm 0.42) \times 10^{13} \text{ cm}^{-2}$ ,  $(2.84 \pm 0.47) \times 10^{13} \text{ cm}^{-2}$ , and  $(0.82 \pm 0.15) \times 10^{13} \text{ cm}^{-2}$  for Maser-only, Maser-RRL, and RRL-only sources, respectively. Based on the FIR data obtained from Hi-GAL and ATLASGAL, we constructed the FIR SED for our sample and obtained a number of physical parameters by fitting the SED, including the dust temperature, the  $H_2$  column density, and the relative abundance of cyanopolyynes. The mean relative abundances of  $HC_3N$  are  $(1.22 \pm 0.52) \times 10^{-10}$ ,  $(5.40 \pm 1.45) \times 10^{-10}$ , and  $(1.65 \pm 1.50) \times 10^{-10}$  for Maser-only, Maser-RRL, and RRL-only sources, respectively.
3. The detection rate, the mean column density, and the mean relative abundance of  $HC_3N$  for three types of our sources show the same trend, that is, an increase from Maser-only to Maser-RRL sources and a decrease from Maser-RRL to RRL-only ones. This trend is consistent with the proposed evolutionary trend of  $HC_3N$  (e.g. Urquhart et al. 2019; Yu et al. 2019) under the assumption that our Maser-only, Maser-RRL, and RRL-only sources correspond to YSOs, UC HII regions, and normal classical HII regions, respectively.
4. Our statistical analysis of the integrated line intensity and the column density of  $HC_3N$  and shock-tracing molecules ( $SiO$ ,  $H_2CO$ ) enabled us to find positive correlations between them. Such findings suggest that  $HC_3N$  may be another tracer of shock. This supports the results of chemical models put forward by Taniguchi et al. (2019a), which suggest that the sublimation of  $CH_4$  and  $C_2H_2$  from dust grains enhances key reactions of the formation of cyanopolyynes. We indirectly show that the neutral–neutral reaction between  $C_2H_2$  and  $CN$  is the dominant formation pathway of  $HC_3N$ .
5. We detect  $HC_5N$  in 11 HMSFRs with a formed protostar, including 2 Maser-only and 9 Maser-RRL sources. Among these 11 sources, 10 sources are new detections (except G24.790+0.084). We detect  $HC_7N$  in G24.790+0.084, which results in three  $HC_7N$  sources in HMSFRs with a formed protostar. Our detections enlarge the samples of

$HC_5N$  and  $HC_7N$  and support the idea that unsaturated iCOMs can exist in YSOs and UC HII regions.

*Acknowledgements.* This work is supported by the Natural Science Foundation of China (No. 12041302, 11590782). We thank the operators and staff at the TMRT stations for their assistance during our observations. We also thank Dr. J.Z. Wang, Dr. X.D. Tang and Dr. X. Chen for their nice comments and suggestions. Y. T. Y. is a member of the International Max Planck Research School (IM-PRS) for Astronomy and Astrophysics at the Universities of Bonn and Cologne. Y. T. Y. would like to thank the China Scholarship Council (CSC) for support. J. J. Q. thanks for support from the NSFC (No. 12003080), the China Postdoctoral Science Foundation funded project (No. 2019M653144), the Guangdong Basic and Applied Basic Research Foundation (No. 2019A1515110588), and the Fundamental Research Funds for the Central Universities, Sun Yat-sen University (No. 2021qntd28). The authors would like to express their gratitude to EditSprings (<https://www.editsprings.cn>) for the expert linguistic services provided.

## References

Aikawa, Y., Wakelam, V., Garrod, R. T., & Herbst, E. 2008, *ApJ*, 674, 984  
 Anderson, L. D., Armentrout, W. P., Luisi, M., et al. 2018, *ApJS*, 234, 33  
 Anderson, L. D., Bania, T. M., Balser, D. S., et al. 2014, *ApJS*, 212, 1  
 Anderson, L. D., Bania, T. M., Balser, D. S., & Rood, R. T. 2011, *ApJS*, 194, 32  
 Araki, M., Takano, S., Sakai, N., et al. 2016, *ApJ*, 833, 291  
 Arce, H. G., Santiago-García, J., Jørgensen, J. K., Tafalla, M., & Bachiller, R. 2008, *ApJ*, 681, L21  
 Bell, M. B., Feldman, P. A., Travers, M. J., et al. 1997, *ApJ*, 483, L61  
 Belloche, A., Müller, H. S. P., Menten, K. M., Schilke, P., & Comito, C. 2013, *A&A*, 559, A47  
 Beltrán, M. T., Gueth, F., Guilloteau, S., & Dutrey, A. 2004, *A&A*, 416, 631  
 Benedettini, M., Viti, S., Codella, C., et al. 2013, *MNRAS*, 436, 179  
 Bernasconi, P. A. & Maeder, A. 1996, *A&A*, 307, 829  
 Breen, S. L., Ellingsen, S. P., Caswell, J. L., & Lewis, B. E. 2010, *MNRAS*, 401, 2219  
 Busso, S. 2012, in *AAS Meeting*, Vol. 219, 446.10  
 Calcutt, H., Fiechter, M. R., Willis, E. R., et al. 2018, *A&A*, 617, A95  
 Ceccarelli, C., Caselli, P., Fontani, F., et al. 2017, *ApJ*, 850, 176  
 Cernicharo, J., Marcelino, N., Agúndez, M., et al. 2020, *A&A*, 642, L8  
 Cesaroni, R. 2005, in *Massive Star Birth: A Crossroads of Astrophysics*, Vol. 227, 59–69  
 Chapman, J. F., Millar, T. J., Wardle, M., Burton, M. G., & Walsh, A. J. 2009, *MNRAS*, 394, 221  
 Chen, H.-Y., Chen, X., Wang, J.-Z., Shen, Z.-Q., & Yang, K. 2020, *ApJS*, 248, 3  
 Chira, R. A., Beuther, H., Linz, H., et al. 2013, *A&A*, 552, A40  
 Chung, H. S., Osamu, K., & Masaki, M. 1991, *JKAS*, 24, 217  
 Churchwell, E. 2002, *ARA&A*, 40, 27  
 Codella, C., Bachiller, R., & Reipurth, B. 1999, *A&A*, 343, 585  
 Codella, C., Lefloch, B., Ceccarelli, C., et al. 2010, *A&A*, 518, L112  
 Condon, J. J. & Ransom, S. M. 2016, *Essential Radio Astronomy*, Vol. 4.3, 6–18  
 Contreras, Y., Schuller, F., Urquhart, J. S., et al. 2013, *A&A*, 549, A45  
 Cosentino, G., Jiménez-Serra, I., Henshaw, J. D., et al. 2018, *MNRAS*, 474, 3760  
 Csengeri, T., Leurini, S., Wyrowski, F., et al. 2016, *A&A*, 586, A149  
 Cummings, S. E., Linke, R. A., & Thaddeus, P. 1986, *ApJS*, 60, 819  
 Cyganowski, C. J., Koda, J., Rosolowsky, E., et al. 2013, *ApJ*, 764, 61  
 Duarte-Cabral, A., Bontemps, S., Motte, F., et al. 2014, *A&A*, 570, A1  
 Elia, D., Schisano, E., Molinari, S., et al. 2010, *A&A*, 518, L97  
 Ellingsen, S. P. 2006, *ApJ*, 638, 241  
 Ellingsen, S. P. 2007, *MNRAS*, 377, 571  
 Esplugues, G. B., Cernicharo, J., Viti, S., et al. 2013, *A&A*, 559, A51  
 Feng, H., Wang, J., Li, S., et al. 2021, *PASJ*, 73, 467  
 Feng, S., Beuther, H., Henning, T., et al. 2015, *A&A*, 581, A71  
 Garrod, R. T. & Herbst, E. 2006, *A&A*, 457, 927  
 Gerner, T., Beuther, H., Semenov, D., et al. 2014, *A&A*, 563, A97  
 Giannetti, A., Leurini, S., König, C., et al. 2017, *A&A*, 606, L12  
 Gieser, C., Beuther, H., Semenov, D., et al. 2021, *A&A*, 648, A66  
 Goldsmith, P. F. & Langer, W. D. 1999, *ApJ*, 517, 209  
 Gong, Y., Henkel, C., Thorwirth, S., et al. 2015, *A&A*, 581, A48  
 Graninger, D. M., Wilkins, O. H., & Öberg, K. I. 2016, *ApJ*, 819, 140  
 Gravity Collaboration, Abuter, R., Amorim, A., et al. 2018, *A&A*, 615, L15  
 Green, C. E., Green, J. A., Burton, M. G., et al. 2014, *MNRAS*, 443, 2252  
 Gusdorf, A., Cabrit, S., Flower, D. R., & Pineau Des Forets, G. 2008, *A&A*, 482, 809  
 Güsten, R., Nyman, L. Å., Schilke, P., et al. 2006, *A&A*, 454, L13  
 Guzmán, A. E., Sanhueza, P., Contreras, Y., et al. 2015, *ApJ*, 815, 130  
 Hassel, G. E., Herbst, E., & Garrod, R. T. 2008, *ApJ*, 681, 1385  
 He, Y.-X., Henkel, C., Zhou, J.-J., et al. 2021, *ApJS*, 253, 2  
 Herbst, E. & van Dishoeck, E. F. 2009, *ARA&A*, 47, 427

Hirota, T., Ohishi, M., & Yamamoto, S. 2009, *ApJ*, 699, 585  
 Hoq, S., Jackson, J. M., Foster, J. B., et al. 2013, *ApJ*, 777, 157  
 Hosokawa, T., & Omukai, K. 2009, *ApJ*, 691, 823  
 Jørgensen, J. K., Belloche, A., & Garrod, R. T. 2020, *ARA&A*, 58, 727  
 Kauffmann, J., Bertoldi, F., Bourke, T. L., Evans, N. J., I., & Lee, C. W. 2008, *A&A*, 487, 993  
 König, C., Urquhart, J. S., Csengeri, T., et al. 2017, *A&A*, 599, A139  
 Kurtz, S., Cesaroni, R., Churchwell, E., Hofner, P., & Walmsley, C. M. 2000, in *Protostars and Planets IV*, 299–326  
 Law, C. J., Öberg, K. I., Bergner, J. B., & Graninger, D. 2018, *ApJ*, 863, 88  
 Levshakov, S. A., Lapinov, A. V., Henkel, C., et al. 2010, *A&A*, 524, A32  
 Li, F. C., Xu, Y., Wu, Y. W., et al. 2016, *AJ*, 152, 92  
 Li, J., Shen, Z.-Q., Wang, J., et al. 2016, *ApJ*, 824, 136  
 Liu, H.-L., Liu, T., Evans, Neal J., I., et al. 2021, *MNRAS*, 505, 2801  
 Loomis, R. A., Shingledecker, C. N., Langston, G., et al. 2016, *MNRAS*, 463, 4175  
 López-Sepulcre, A., Watanabe, Y., Sakai, N., et al. 2016, *ApJ*, 822, 85  
 Luisi, M., Anderson, L. D., Bania, T. M., et al. 2018, *PASP*, 130, 084101  
 Mangum, J. G. & Shirley, Y. L. 2015, *PASP*, 127, 266  
 Martin-Pintado, J., Bachiller, R., & Fuente, A. 1992, *A&A*, 254, 315  
 McCarthy, M. C., Grabow, J. U., Travers, M. J., et al. 1998, *ApJ*, 494, L231  
 McElroy, D., Walsh, C., Markwick, A. J., et al. 2013, *A&A*, 550, A36  
 McGee, R. X., Newton, L. M., & Butler, P. W. 1975, *ApJ*, 202, 76  
 Mendoza, E., Lefloch, B., Ceccarelli, C., et al. 2018, *MNRAS*, 475, 5501  
 Miettinen, O. 2014, *A&A*, 562, A3  
 Minier, V., Ellingsen, S. P., Norris, R. P., & Booth, R. S. 2003, *A&A*, 403, 1095  
 Mitchell, G. F. 1984, *ApJS*, 54, 81  
 Molinari, S., Pezzuto, S., Cesaroni, R., et al. 2008, *A&A*, 481, 345  
 Molinari, S., Schisano, E., Elia, D., et al. 2016, *A&A*, 591, A149  
 Newville, M., Stensitzki, T., Allen, D. B., et al. 2016, *ASCL*  
 Ossenkopf, V. & Henning, T. 1994, *A&A*, 291, 943  
 Ragan, S. E., Bergin, E. A., & Wilner, D. 2011, *ApJ*, 736, 163  
 Rathborne, J. M., Garay, G., Jackson, J. M., et al. 2011, *ApJ*, 741, 120  
 Reid, M. J., Menten, K. M., Brunthaler, A., et al. 2019, *ApJ*, 885, 131  
 Reid, M. J., Menten, K. M., Brunthaler, A., et al. 2014, *ApJ*, 783, 130  
 Rolfs, R., Schilke, P., Zhang, Q., & Zapata, L. 2011, *A&A*, 536, A33  
 Roman-Duval, J., Jackson, J. M., Heyer, M., et al. 2009, *ApJ*, 699, 1153  
 Sabatini, G., Bovino, S., Giannetti, A., et al. 2021, *A&A*, 652, A71  
 Sakai, N., Ikeda, M., Morita, M., et al. 2007, *ApJ*, 663, 1174  
 Sakai, N., Sakai, T., Hirota, T., & Yamamoto, S. 2009, *ApJ*, 702, 1025  
 Sakai, N., Sakai, T., Hirota, T., & Yamamoto, S. 2010, *ApJ*, 722, 1633  
 Sakai, T., Sakai, N., Kamegai, K., et al. 2008, *ApJ*, 678, 1049  
 Schuller, F., Menten, K. M., Contreras, Y., et al. 2009, *A&A*, 504, 415  
 Shirley, Y. L. 2015, *PASP*, 127, 299  
 Sobolev, A. M., & Deguchi, S. 1994, *A&A*, 291, 569  
 Suzuki, H., Yamamoto, S., Ohishi, M., et al. 1992, *ApJ*, 392, 551  
 Svoboda, B. E., Shirley, Y. L., Battersby, C., et al. 2016, *ApJ*, 822, 59  
 Tafalla, M., Myers, P. C., Caselli, P., & Walmsley, C. M. 2004, *A&A*, 416, 191  
 Tafalla, M., Santiago-García, J., Hacar, A., & Bachiller, R. 2010, *A&A*, 522, A91  
 Takano, S., Masuda, A., Hirahara, Y., et al. 1998, *A&A*, 329, 1156  
 Tang, X. D., Henkel, C., Wyrowski, F., et al. 2018, *A&A*, 611, A6  
 Taniguchi, K., Herbst, E., Caselli, P., et al. 2019a, *ApJ*, 881, 57  
 Taniguchi, K., Miyamoto, Y., Saito, M., et al. 2018a, *ApJ*, 866, 32  
 Taniguchi, K., Saito, M., Majumdar, L., et al. 2018b, *ApJ*, 866, 150  
 Taniguchi, K., Saito, M., & Ozeki, H. 2016, *ApJ*, 830, 106  
 Taniguchi, K., Saito, M., Sridharan, T. K., & Minamidani, T. 2018c, *ApJ*, 854, 133  
 Taniguchi, K., Saito, M., Sridharan, T. K., & Minamidani, T. 2019b, *ApJ*, 872, 154  
 Thaddeus, P. & McCarthy, M. C. 2001, *SAA*, 57, 757  
 Travers, M. J., McCarthy, M. C., Kalmus, P., Gottlieb, C. A., & Thaddeus, P. 1996, *ApJ*, 469, L65  
 Urquhart, J. S., Csengeri, T., Wyrowski, F., et al. 2014a, *A&A*, 568, A41  
 Urquhart, J. S., Figura, C., Wyrowski, F., et al. 2019, *MNRAS*, 484, 4444  
 Urquhart, J. S., König, C., Giannetti, A., et al. 2018, *MNRAS*, 473, 1059  
 Urquhart, J. S., Moore, T. J. T., Csengeri, T., et al. 2014b, *MNRAS*, 443, 1555  
 Urquhart, J. S., Morgan, L. K., Figura, C. C., et al. 2011, *MNRAS*, 418, 1689  
 Urquhart, J. S., Wells, M. R. A., Pillai, T., et al. 2022, *MNRAS*, 510, 3389  
 Viti, S., Jimenez-Serra, I., Yates, J. A., et al. 2011, *ApJ*, 740, L3  
 Wakelam, V., Caselli, P., Ceccarelli, C., Herbst, E., & Castets, A. 2004, *A&A*, 422, 159  
 Walsh, A. J., Burton, M. G., Hyland, A. R., & Robinson, G. 1998, *MNRAS*, 301, 640  
 Wang, J. Q., Yu, L. F., Jiang, Y. B., et al. 2017, *AcASn*, 58, 37  
 Wang, S., Ren, Z., Li, D., et al. 2020, *MNRAS*, 499, 4432  
 Widicus Weaver, S. L., Laas, J. C., Zou, L., et al. 2017, *ApJS*, 232, 3  
 Wienen, M., Wyrowski, F., Schuller, F., et al. 2012, *A&A*, 544, A146  
 Wu, Y., Liu, X., Chen, X., et al. 2019, *MNRAS*, 488, 495  
 Xu, Y., Li, J. J., Hachisuka, K., et al. 2008, *A&A*, 485, 729  
 Yang, K., Chen, X., Shen, Z.-Q., et al. 2019, *ApJS*, 241, 18  
 Yang, K., Chen, X., Shen, Z.-Q., et al. 2017, *ApJ*, 846, 160  
 Yang, T., Chen, X., Ouyang, X. J., & Zhang, Y. K. in prep.  
 Yu, N. & Wang, J.-J. 2015, *MNRAS*, 451, 2507  
 Yu, N., Wang, J.-J., & Xu, J.-L. 2019, *MNRAS*, 489, 4497  
 Yu, N. & Xu, J. 2016, *ApJ*, 833, 248  
 Zhang, C., Evans, N. J., Liu, T., et al. 2022, *MNRAS*, 510, 4998  
 Zhang, C., Wu, Y., Liu, X. C., et al. 2021, *A&A*, 648, A83  
 Zhang, X.-Y., Zhu, Q.-F., Li, J., et al. 2017, *A&A*, 606, A74  
 Zhang, Y.-J., Zhou, J.-J., Esimbek, J., et al. 2016, *Ap&SS*, 361, 191

**Table 1.** Summary of target lines.

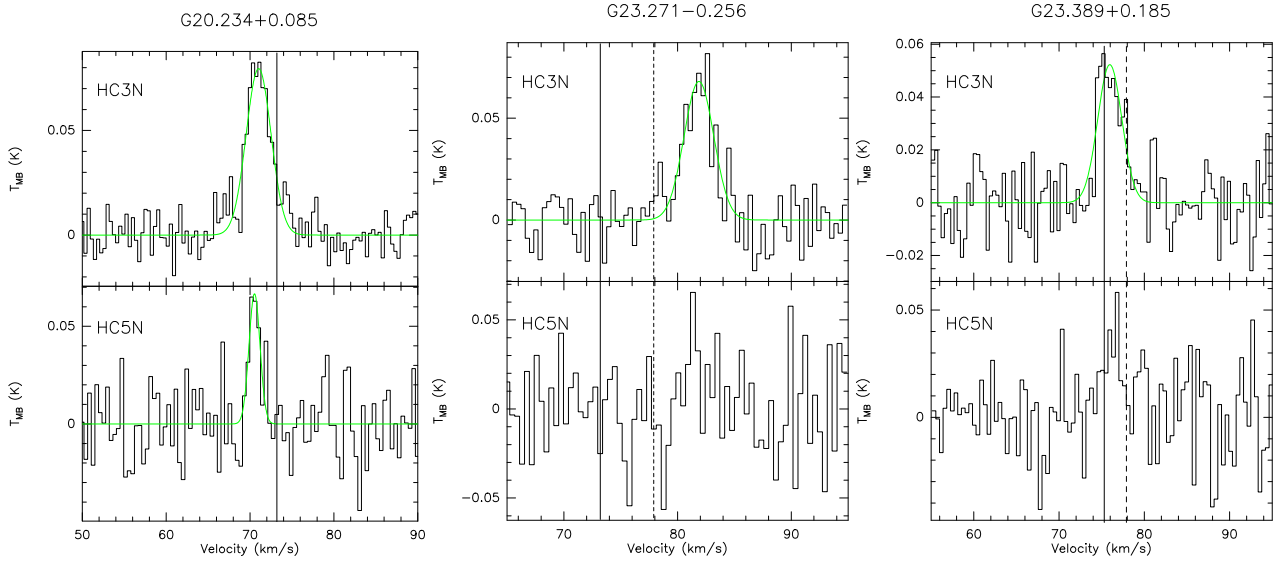
Species (1)	Transition (2)	Frequency (MHz) (3)	$S\mu^2$ (Debye <sup>2</sup> ) (4)	$E_u/k$ (K) (5)	HPBW (") (6)
HC <sub>3</sub> N	J = 2-1, F = 2-2	18194.92	2.32	1.3	52
	J = 2-1, F = 1-0	18195.14	3.09	1.3	52
	J = 2-1, F = 2-1	18196.22	6.96	1.3	52
	J = 2-1, F = 3-2	18196.31	13.00	1.3	52
	J = 2-1, F = 1-2	18197.08	0.18	1.3	52
	J = 2-1, F = 1-1	18198.38	2.32	1.3	52
HC <sub>5</sub> N	J = 6-5	15975.93	337.45	2.68	60
HC <sub>7</sub> N	J = 15-14	16919.98	1045.44	6.50	56

**Notes.** (1): Molecular species; (2): Transition; (3): Rest frequency; (4-5): The product of the line strength and the square of the electric dipole moment and the upper level energy in K, which are taken from CDMS; (6): Half power beam width.

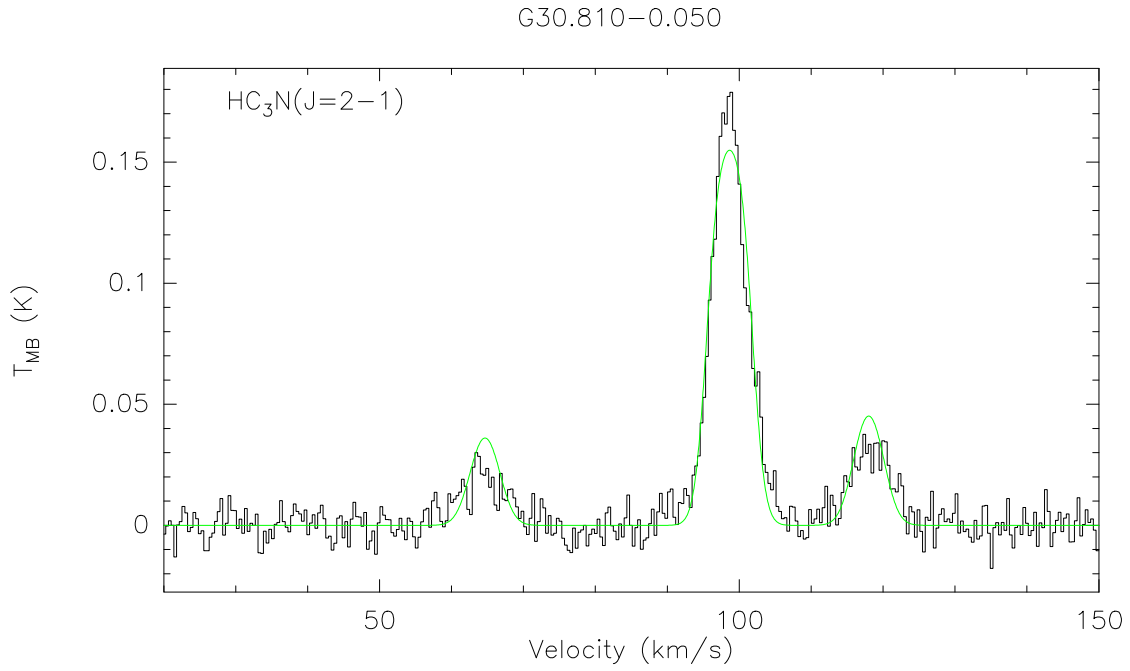
**Table 2.** Far infrared properties of our  $\text{HC}_3\text{N}$  sources.

Classifications	Source Name	$F_{70}$ (Jy)	$F_{160}$ (Jy)	$F_{250}$ (Jy)	$F_{350}$ (Jy)	$F_{500}$ (Jy)	$F_{870}$ (Jy)	$R_{\text{eff}}$ (")	$\gamma$	$T_{\text{dust}}$ (K)	$M$ ( $M_{\odot}$ )	$T_{\text{dust}}^a$ (K)	$M^a$ ( $M_{\odot}$ )	$N(\text{H}_2)$ ( $10^{23} \text{ cm}^{-2}$ )
(1)	(2)	(3)	(4)	(5)	(6)	(7)	(8)	(9)	(10)	(11)	(12)	(13)	(14)	(15)
Maser-only	G20.234+0.085	47 $\pm$ 1	176 $\pm$ 4	157 $\pm$ 5	66 $\pm$ 1	35 $\pm$ 1	5 $\pm$ 1	27	65	17.26 $\pm$ 0.76	593 $\pm$ 115	21.4	687	1.84 $\pm$ 0.05
	G23.484+0.097	144 $\pm$ 4	257 $\pm$ 6	282 $\pm$ 10	110 $\pm$ 4	58 $\pm$ 4	12 $\pm$ 2	41	63	16.09 $\pm$ 1.04	1571 $\pm$ 462	21.4	2148	0.71 $\pm$ 0.02
	G25.649+1.050	1140 $\pm$ 48	1053 $\pm$ 21	752 $\pm$ 4	413 $\pm$ 10	177 $\pm$ 6	39 $\pm$ 6	55	75	18.38 $\pm$ 0.16	4122 $\pm$ 155	23.4	743	1.06 $\pm$ 0.03
	G28.817+0.365	156 $\pm$ 8	256 $\pm$ 5	298 $\pm$ 10	91 $\pm$ 1	43 $\pm$ 1	8 $\pm$ 1	29	71	16.35 $\pm$ 1.63	1381 $\pm$ 624	23.0	807	1.47 $\pm$ 0.03
	G30.770-0.804	73 $\pm$ 3	87 $\pm$ 2	76 $\pm$ 2	33 $\pm$ 2	22 $\pm$ 1	4 $\pm$ 1	24	79	17.20 $\pm$ 0.75	259 $\pm$ 50	19.8	399	2.77 $\pm$ 0.09
	G37.043-0.035	25 $\pm$ 1	57 $\pm$ 1	64 $\pm$ 3	40 $\pm$ 2	13 $\pm$ 1	3 $\pm$ 1	5	79	15.03 $\pm$ 0.41	548 $\pm$ 69	18.0	695	67.87 $\pm$ 1.58
Maser-RRL	G23.271-0.256	70 $\pm$ 2	104 $\pm$ 3	235 $\pm$ 12	132 $\pm$ 5	81 $\pm$ 4	25 $\pm$ 4	62	56	12.40 $\pm$ 0.80	4922 $\pm$ 1520	19.3	3020	0.40 $\pm$ 0.01
	G23.389+0.185	270 $\pm$ 13	173 $\pm$ 3	181 $\pm$ 4	83 $\pm$ 1	43 $\pm$ 1	9 $\pm$ 2	29	64	15.94 $\pm$ 0.66	1055 $\pm$ 201	20.2	2612	1.28 $\pm$ 0.03
	G23.436-0.184	147 $\pm$ 4	446 $\pm$ 20	630 $\pm$ 28	253 $\pm$ 9	128 $\pm$ 4	40 $\pm$ 6	51	57	14.77 $\pm$ 1.16	5997 $\pm$ 2200	24.6	5702	0.36 $\pm$ 0.01
	G23.965-0.110	207 $\pm$ 9	336 $\pm$ 7	377 $\pm$ 9	152 $\pm$ 4	83 $\pm$ 2	20 $\pm$ 3	49	62	15.86 $\pm$ 0.97	2330 $\pm$ 648	20.1	4169	0.43 $\pm$ 0.01
	G24.328+0.144	523 $\pm$ 20	810 $\pm$ 16	623 $\pm$ 1	253 $\pm$ 6	116 $\pm$ 2	17 $\pm$ 3	43	57	18.68 $\pm$ 0.75	4076 $\pm$ 695	23.8	4416	0.29 $\pm$ 0.01
	G24.790+0.084	2000 $\pm$ 300	3000 $\pm$ 600	1000 $\pm$ 200	600 $\pm$ 100	200 $\pm$ 100	57 $\pm$ 9	42	55	32.10 $\pm$ 3.89	1639 $\pm$ 571	26.5	7638	0.53 $\pm$ 0.01
	G25.709+0.044	352 $\pm$ 17	431 $\pm$ 9	473 $\pm$ 18	140 $\pm$ 8	64 $\pm$ 1	9 $\pm$ 2	28	59	16.77 $\pm$ 1.69	2844 $\pm$ 128	29.0	2041	1.02 $\pm$ 0.02
	G28.147-0.004	129 $\pm$ 6	148 $\pm$ 4	184 $\pm$ 4	66 $\pm$ 1	38 $\pm$ 1	9 $\pm$ 2	33	60	15.55 $\pm$ 1.27	1773 $\pm$ 665	22.2	1596	0.41 $\pm$ 0.02
	G28.393+0.085	73 $\pm$ 9	300 $\pm$ 16	416 $\pm$ 14	214 $\pm$ 9	140 $\pm$ 4	12 $\pm$ 2	41	72	14.11 $\pm$ 0.66	3590 $\pm$ 798	18.5	2189	0.31 $\pm$ 0.02
	G29.835-0.012	337 $\pm$ 16	251 $\pm$ 7	213 $\pm$ 13	101 $\pm$ 5	60 $\pm$ 5	13 $\pm$ 2	37	62	17.17 $\pm$ 0.53	2491 $\pm$ 337	29.6	1119	0.89 $\pm$ 0.02
	G30.897+0.163	113 $\pm$ 5	179 $\pm$ 5	252 $\pm$ 6	86 $\pm$ 3	47 $\pm$ 1	18 $\pm$ 3	43	64	15.09 $\pm$ 1.46	3474 $\pm$ 1560	21.0	578	0.70 $\pm$ 0.01
	G31.579+0.076	648 $\pm$ 16	769 $\pm$ 20	647 $\pm$ 18	217 $\pm$ 4	93 $\pm$ 2	13 $\pm$ 2	26	68	18.44 $\pm$ 1.32	2993 $\pm$ 915	27.0	1216	1.43 $\pm$ 0.03
RRL-only	G35.141-0.750	317 $\pm$ 10	642 $\pm$ 17	543 $\pm$ 13	183 $\pm$ 12	139 $\pm$ 4	39 $\pm$ 6	40	100	18.00 $\pm$ 1.26	677 $\pm$ 204	19.4	1086	1.07 $\pm$ 0.02
	G24.546-0.245	64 $\pm$ 3	114 $\pm$ 6	183 $\pm$ 12	105 $\pm$ 6	64 $\pm$ 3	17 $\pm$ 3	55	59	13.27 $\pm$ 0.53	2908 $\pm$ 546	21.1	2904	0.44 $\pm$ 0.02
	G28.452+0.002	133 $\pm$ 5	103 $\pm$ 2	72 $\pm$ 2	30 $\pm$ 2	14 $\pm$ 2	6 $\pm$ 1	29	139	19.47 $\pm$ 0.70	1400 $\pm$ 204	21.6	7047	3.74 $\pm$ 0.17

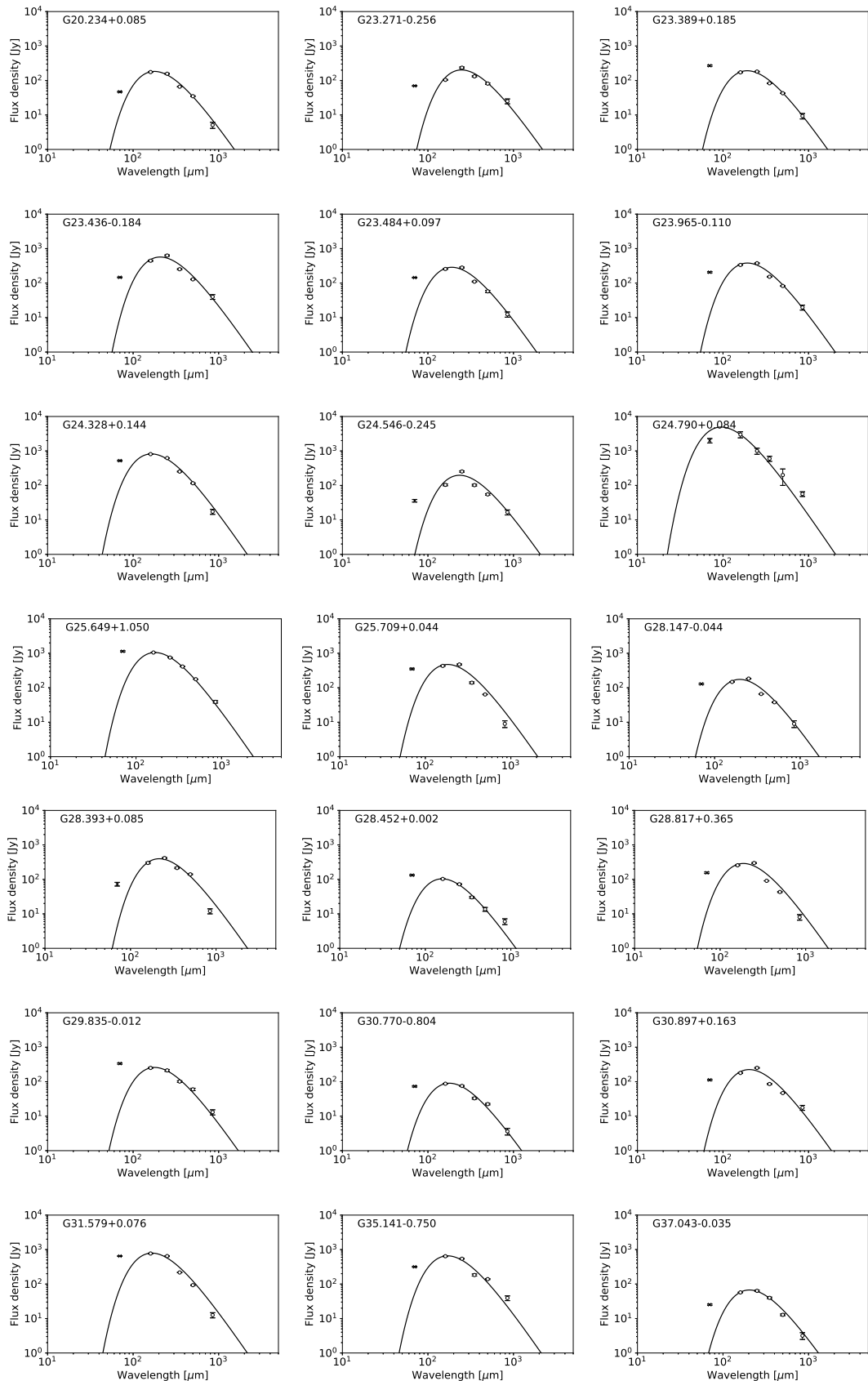
**Notes.** (1): Classifications; (2): Source name; (3-7): Flux density at each band from the Herschel telescope; (8-9): Flux density and effective radius of sources at 870  $\mu\text{m}$  from APEX telescope, which are given by Urquhart et al. (2014a); (10): The gas-to-dust ratio; (11): Dust temperature; (12): Total (gas + dust) core mass; (13-14): Dust temperature and total mass, from Urquhart et al. (2018); (15): Column density of  $\text{H}_2$ .



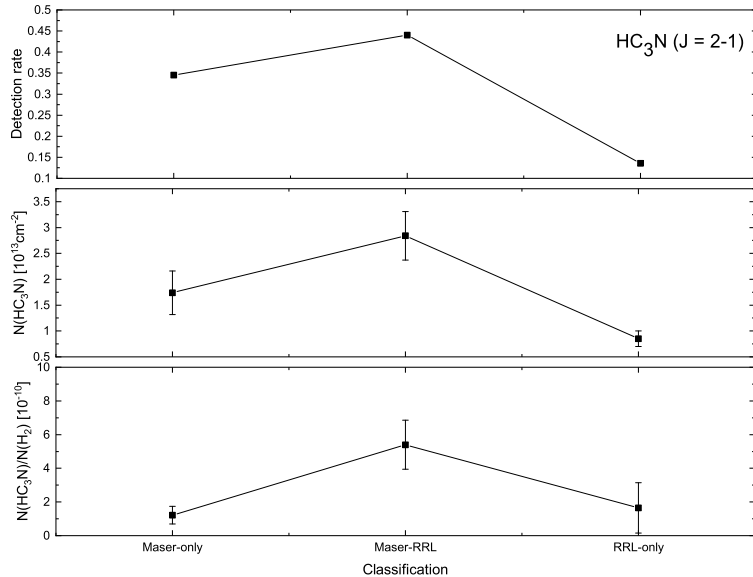
**Fig. 1.** Examples for  $\text{HC}_3\text{N}$ ,  $\text{HC}_5\text{N}$ , and  $\text{HC}_7\text{N}$  with TMRT telescope. Solid and dashed lines show the LSR velocity values of 6.7 GHz  $\text{CH}_3\text{OH}$  maser (Yang et al. 2017, 2019), and of RRL (Chen et al. 2020), respectively. The full spectra are shown in Appendix Fig. A.1.



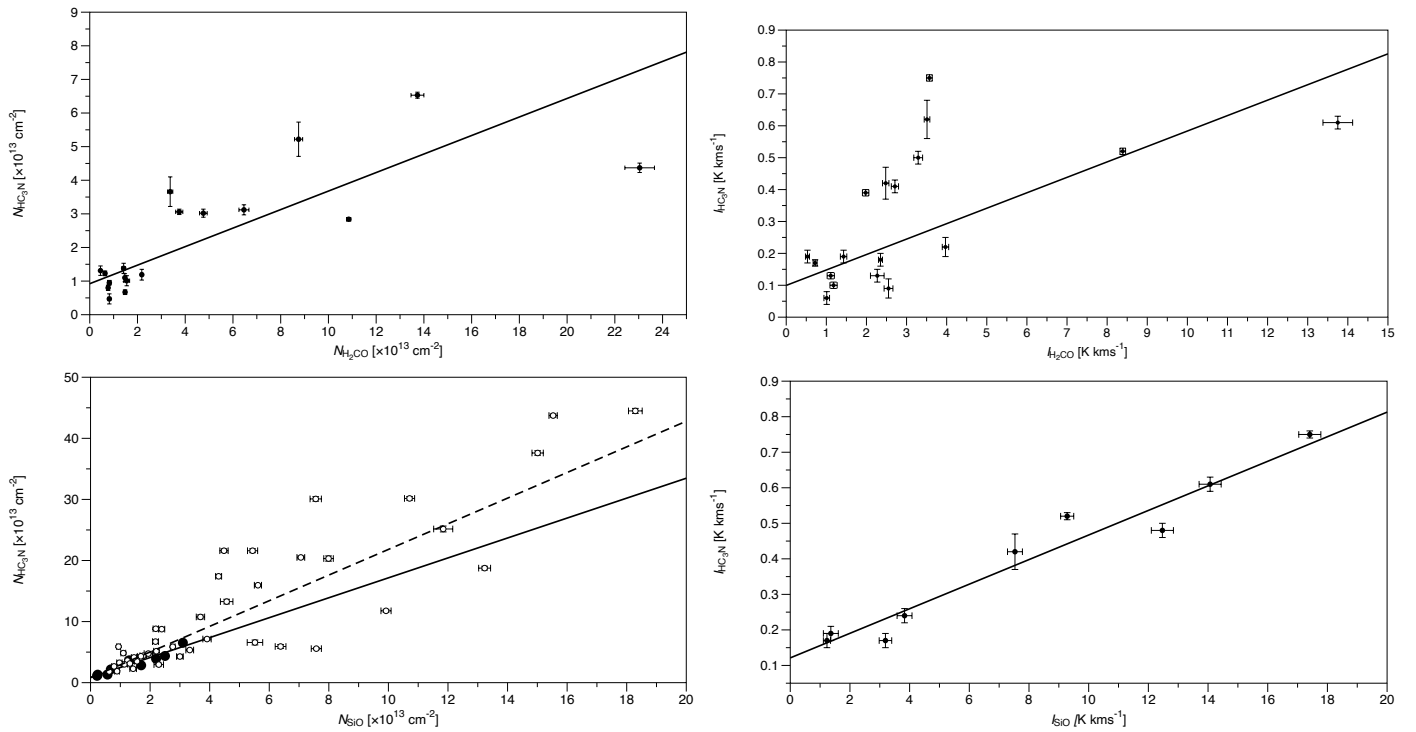
**Fig. 2.** HFS fitting of G30.810-0.050.



**Fig. 3.** FIR SED and its fit curve (the solid curve, from one single temperature grey-body model) of sources with cyanopolyyynes detection. The cross indicates  $70\text{ }\mu\text{m}$  emission, which is not involved in the SED fit.

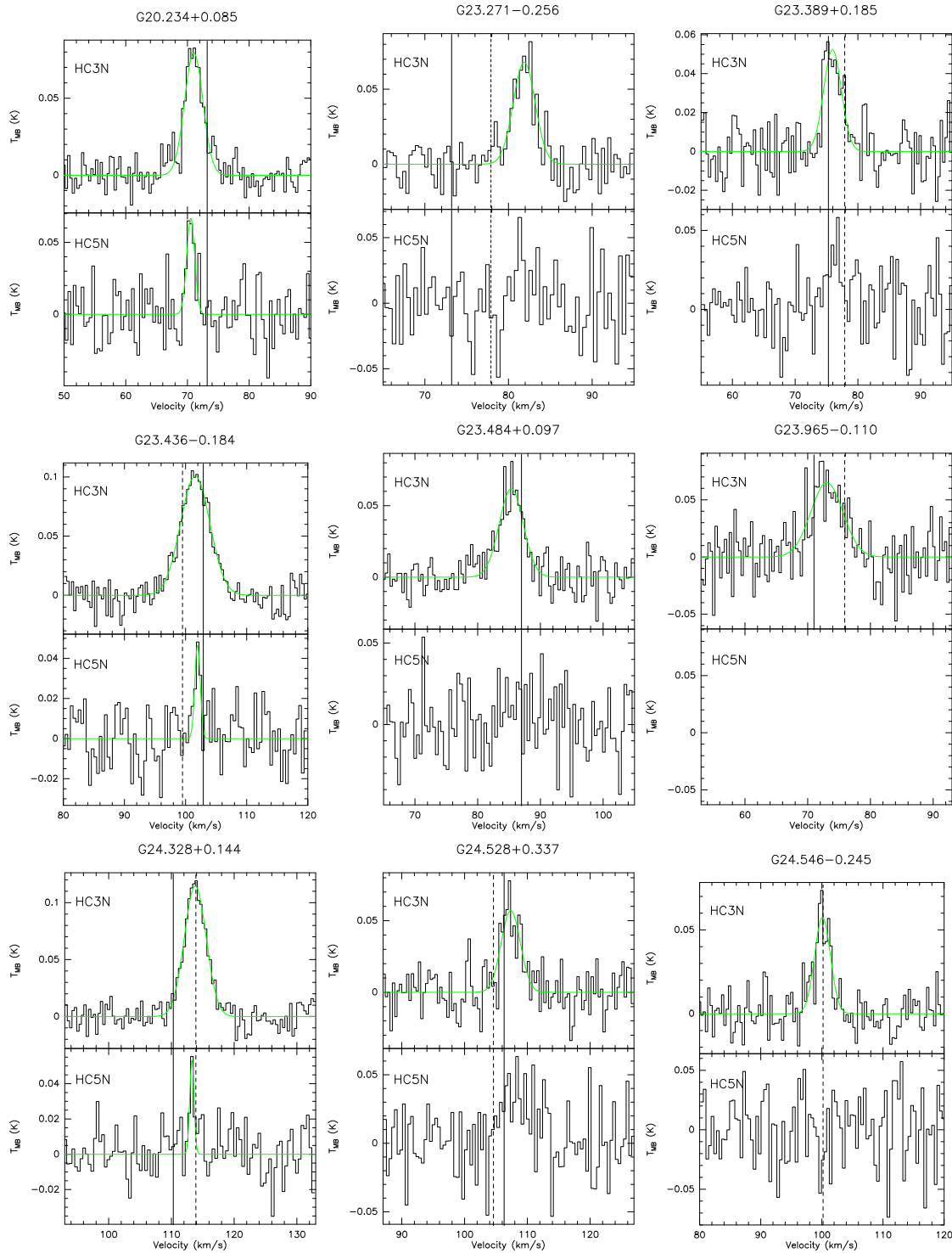


**Fig. 4.** The detection rates, column densities, and relative abundances of  $\text{HC}_3\text{N}$  for different types of sources.

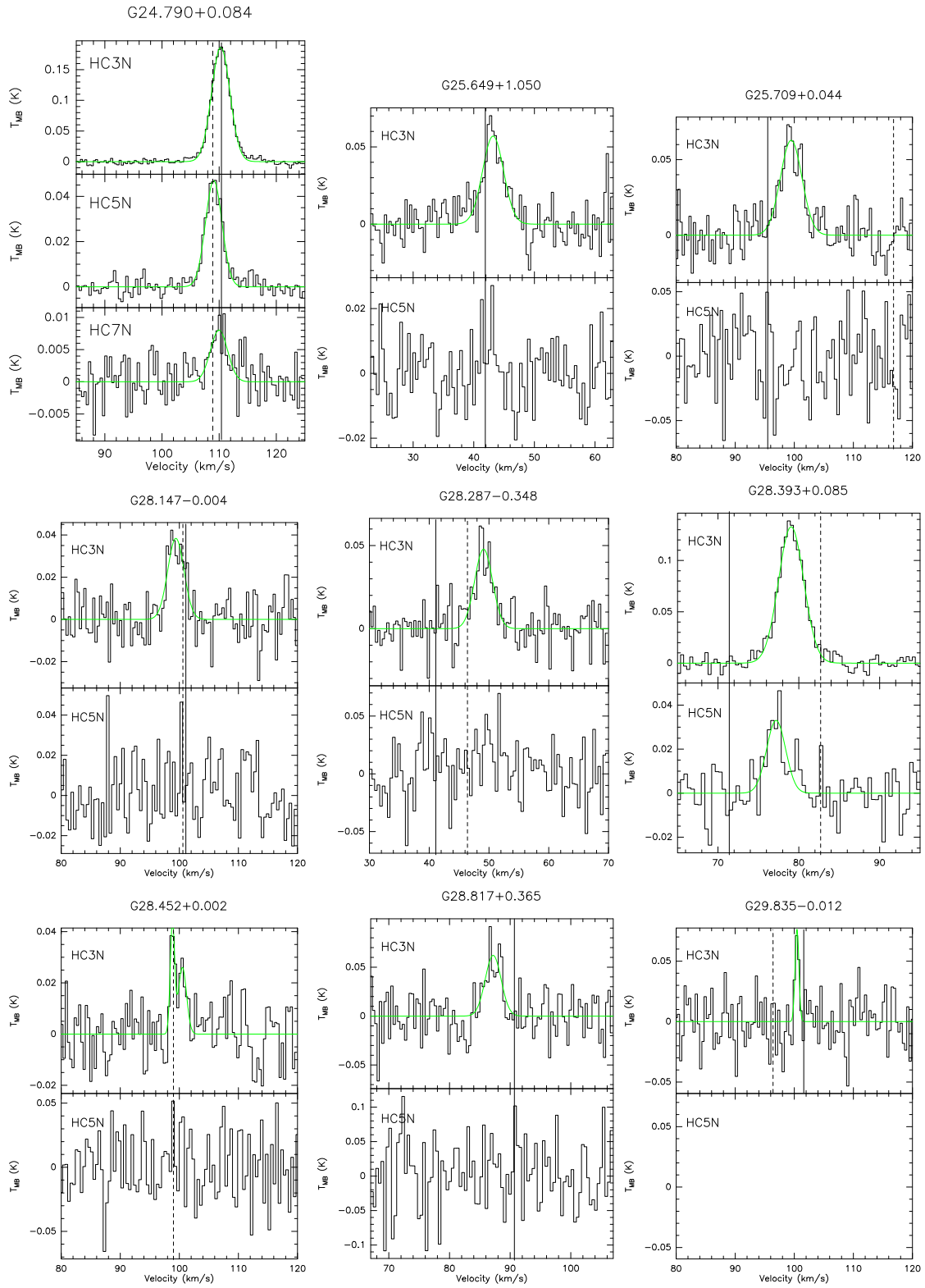


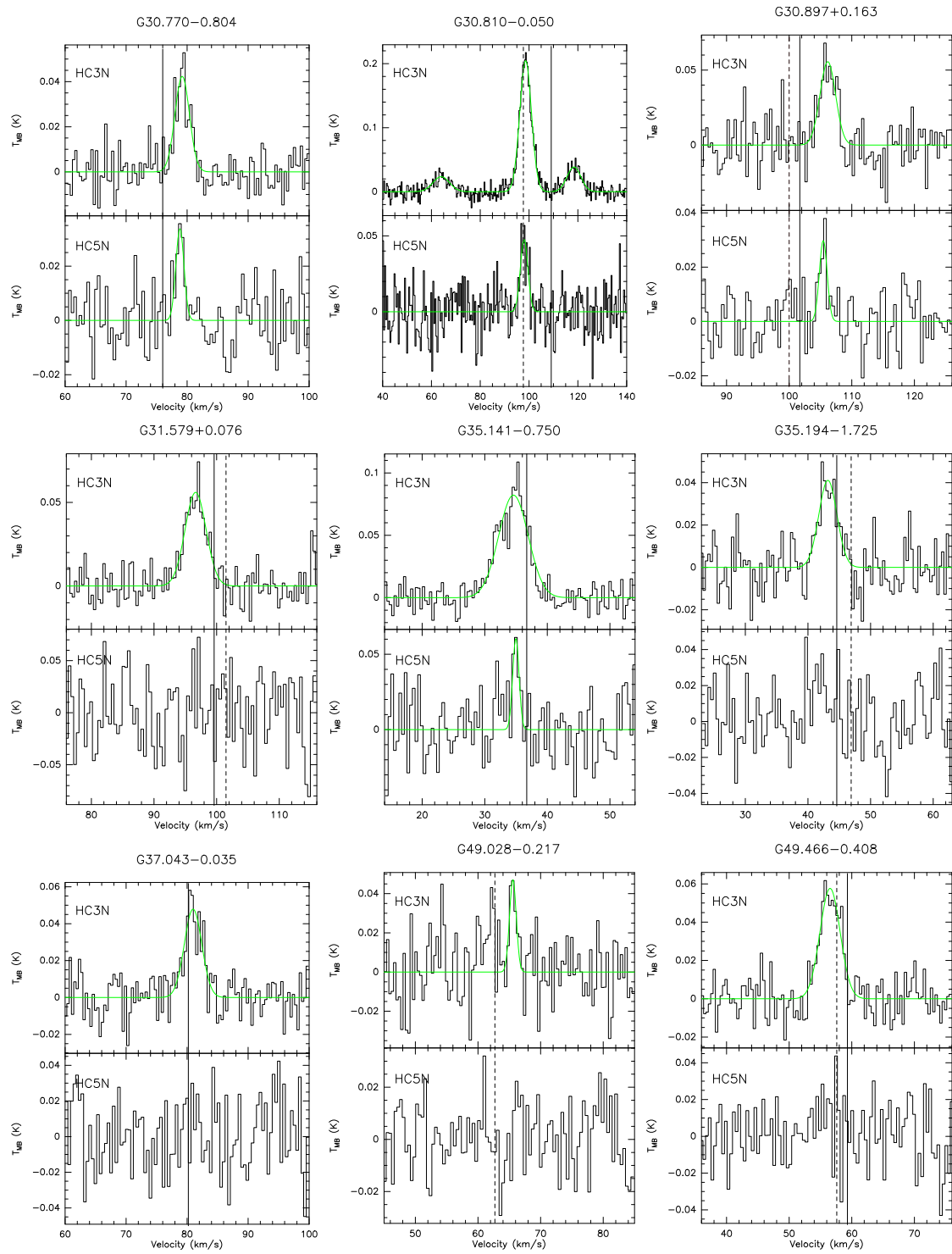
**Fig. 5.** Column density (left panels) and the integrated line intensity (right panels) of  $\text{HC}_3\text{N}$  are plotted against those of shock-tracing molecules ( $\text{H}_2\text{CO}$  and  $\text{SiO}$ ). The circles and empty circles indicate our sources and sources reported in He et al. (2021), respectively. The solid lines and the dashed line show the weighted linear fitting line for our data and theirs.

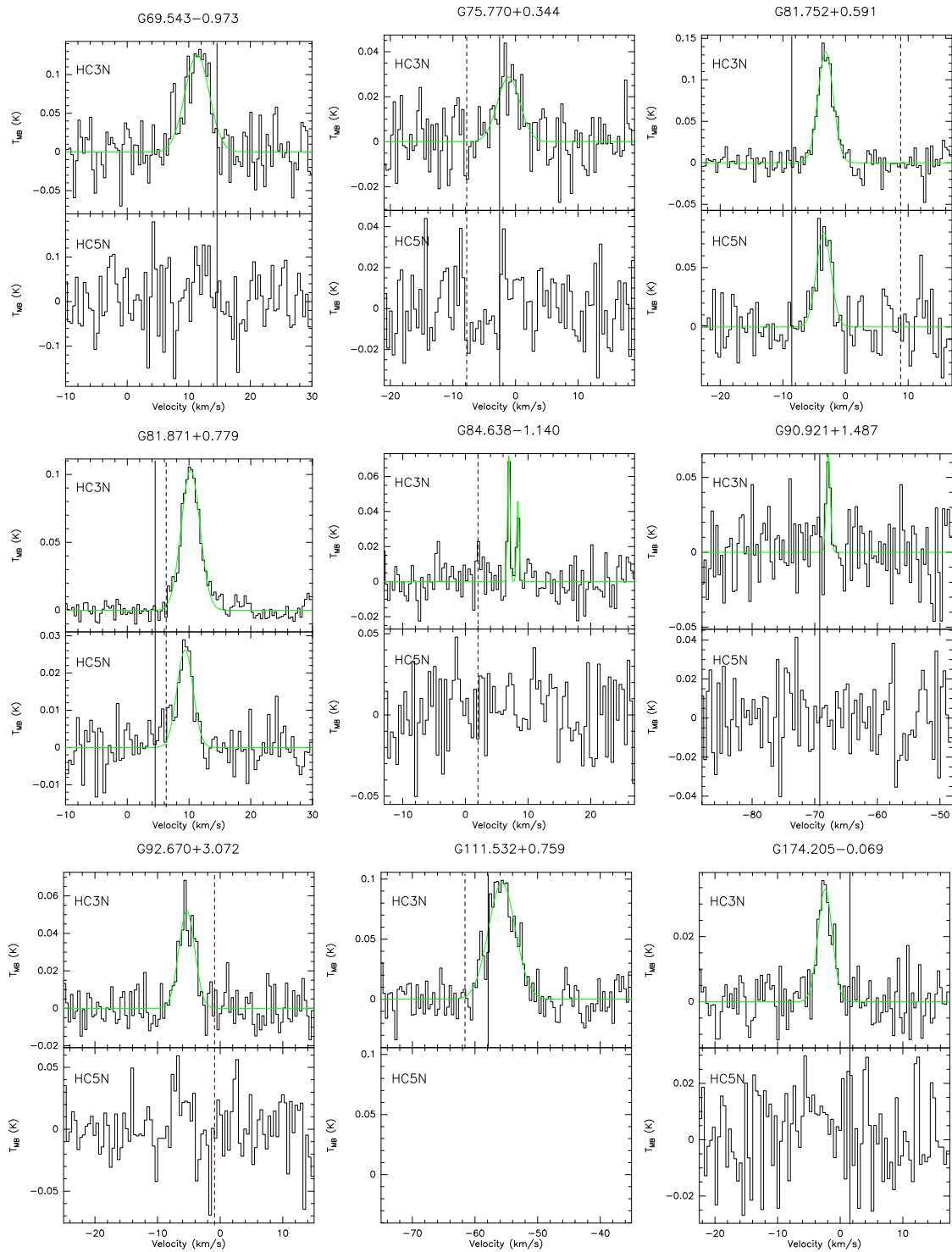
## Appendix A: Spectra of $\text{HC}_3\text{N}$ , $\text{HC}_5\text{N}$ , and $\text{HC}_7\text{N}$

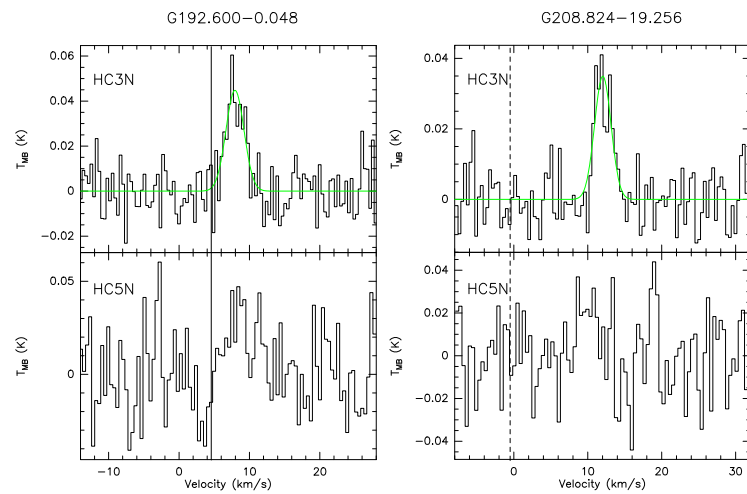


**Fig. A.1.** All spectra for  $\text{HC}_3\text{N}$ ,  $\text{HC}_5\text{N}$ , and  $\text{HC}_7\text{N}$  with TMRT telescope. Solid and dashed lines show the LSR velocity values of the 6.7 GHz  $\text{CH}_3\text{OH}$  maser (Yang et al. 2017, 2019), and of RRL (Chen et al. 2020), respectively. Blank panels represent non-detections.

**Fig. A.1.** Continued.

**Fig. A.1.** Continued.

**Fig. A.1.** Continued.

**Fig. A.1.** Continued.

## Appendix B: The observed properties of detected lines in the survey

**Table B.1.** The  $\text{HC}_3\text{N}$  ( $J = 2-1$ ) transitions detected with the TMRT.

Source Name	R.A. (hh.mm.ss)	DEC (hh.mm.ss)	$V_{LSR}$ (km s $^{-1}$ )	$\Delta\nu$ (km s $^{-1}$ )	$T_{mb}$ (mK)	rms (mK)	$\int T_{mb} d\nu$ (K km s $^{-1}$ )	$D$ (kpc)	$D_{GC}$ (kpc)	Classifications
(1)	(2)	(3)	(4)	(5)	(6)	(7)	(8)	(9)	(10)	(11)
G20.234+0.085	18:27:44.56	-11:14:54.2	71.03 $\pm$ 0.08	3.49 $\pm$ 0.24	80	8	0.30 $\pm$ 0.02	4.41*	4.27	Maser-only
G23.271-0.256	18:34:36.22	-08:42:26.6	81.88 $\pm$ 0.13	3.08 $\pm$ 0.33	68	10	0.22 $\pm$ 0.02	5.92	3.56	Maser-RRL
G23.389+0.185	18:33:14.36	-08:23:57.6	75.96 $\pm$ 0.18	3.33 $\pm$ 0.40	52	12	0.19 $\pm$ 0.02	4.81	4.17	Maser-RRL
G23.436-0.184	18:34:39.21	-08:31:40.4	101.58 $\pm$ 0.11	5.65 $\pm$ 0.25	101	12	0.61 $\pm$ 0.02	5.88	3.59	Maser-RRL
G23.484+0.097	18:33:44.05	-08:21:20.6	85.36 $\pm$ 0.16	4.51 $\pm$ 0.43	62	11	0.30 $\pm$ 0.02	4.93*	4.10	Maser-only
G23.965-0.110	18:35:22.31	-08:01:28.0	73.06 $\pm$ 0.34	6.03 $\pm$ 0.80	65	21	0.42 $\pm$ 0.05	5.07*	4.05	Maser-RRL
G24.328+0.144	18:35:08.15	-07:35:04.4	113.81 $\pm$ 0.07	4.11 $\pm$ 0.17	115	9	0.50 $\pm$ 0.02	7.23*	3.35	Maser-RRL
G24.528+0.337	18:34:49.00	-07:19:05.9	107.36 $\pm$ 0.20	3.59 $\pm$ 0.50	57	13	0.22 $\pm$ 0.03	6.00*	3.65	Maser-RRL
G24.546-0.245	18:36:55.92	-07:34:13.9	100.11 $\pm$ 0.14	3.05 $\pm$ 0.37	57	10	0.19 $\pm$ 0.02	5.70*	3.77	RRL-only
G24.790+0.084	18:36:12.45	-07:12:10.7	110.29 $\pm$ 0.02	3.79 $\pm$ 0.04	186	4	0.75 $\pm$ 0.01	6.67	3.48	Maser-RRL
G25.649+1.050	18:34:20.91	-05:59:42.5	43.19 $\pm$ 0.18	4.08 $\pm$ 0.57	57	12	0.25 $\pm$ 0.03	3.80*	4.98	Maser-only
G25.709+0.044	18:38:03.17	-06:24:15.5	99.47 $\pm$ 0.17	4.32 $\pm$ 0.45	63	12	0.29 $\pm$ 0.02	5.87*	3.81	Maser-RRL
G28.147-0.004	18:42:42.59	-04:15:35.0	99.42 $\pm$ 0.20	3.25 $\pm$ 0.41	38	10	0.13 $\pm$ 0.02	6.33	3.92	Maser-RRL
G28.287-0.348	18:44:11.48	-04:17:32.1	49.11 $\pm$ 0.19	3.52 $\pm$ 0.50	48	11	0.18 $\pm$ 0.02	4.52	4.66	Maser-RRL
G28.393+0.085	18:42:50.49	-04:00:00.0	79.06 $\pm$ 0.04	3.68 $\pm$ 0.09	133	6	0.52 $\pm$ 0.01	4.33	4.78	Maser-RRL
G28.452+0.002	18:43:14.64	-03:59:07.9	98.84 $\pm$ 0.12	0.88 $\pm$ 0.22	43	10	0.04 $\pm$ 0.01	8.17*	8.09	RRL-only
			100.52 $\pm$ 0.26	1.64 $\pm$ 0.74	26		0.05 $\pm$ 0.02			
G28.817+0.365	18:42:37.35	-03:29:41.0	87.21 $\pm$ 0.26	3.09 $\pm$ 0.52	62	21	0.20 $\pm$ 0.03	4.51*	4.70	Maser-only
G29.835-0.012	18:45:59.57	-02:45:04.4	100.46 $\pm$ 0.10	0.76 $\pm$ 0.18	76	20	0.06 $\pm$ 0.02	7.64*	4.09	Maser-RRL
G30.770-0.804	18:50:21.51	-02:17:27.5	79.21 $\pm$ 0.13	2.79 $\pm$ 0.29	42	8	0.13 $\pm$ 0.01	3.71*	5.29	Maser-only
G30.810-0.050	18:47:46.97	-01:54:26.4	64.02 $\pm$ 0.43	7.97 $\pm$ 1.12	24	8	0.20 $\pm$ 0.03	3.12	5.68	Maser-RRL
			98.61 $\pm$ 0.04	5.67 $\pm$ 0.11	204		1.23 $\pm$ 0.02			
			118.42 $\pm$ 0.26	6.72 $\pm$ 0.6	39		0.28 $\pm$ 0.02			
G30.897+0.163	18:47:08.77	-01:44:12.7	106.17 $\pm$ 0.19	2.94 $\pm$ 0.37	56	14	0.17 $\pm$ 0.02	7.07*	4.17	Maser-RRL
G31.579+0.076	18:48:41.94	-01:10:02.5	96.65 $\pm$ 0.14	3.95 $\pm$ 0.34	56	10	0.24 $\pm$ 0.02	5.46	4.50	Maser-RRL
G35.141-0.750	18:58:06.14	01:37:07.5	34.59 $\pm$ 0.11	5.54 $\pm$ 0.25	82	9	0.48 $\pm$ 0.02	2.21*	6.44	Maser-RRL
G35.194-1.725	19:01:42.33	01:13:32.3	43.19 $\pm$ 0.21	3.42 $\pm$ 0.42	41	10	0.15 $\pm$ 0.02	2.43	6.30	Maser-RRL
G37.043-0.035	18:59:03.64	03:37:45.1	80.98 $\pm$ 0.16	3.38 $\pm$ 0.39	48	10	0.17 $\pm$ 0.02	4.57*	5.25	Maser-only
G49.028-0.217	19:22:12.74	14:10:58.3	65.58 $\pm$ 0.20	1.27 $\pm$ 0.41	47	15	0.06 $\pm$ 0.02	5.49*	6.13	RRL-only
G49.466-0.408	19:23:45.73	14:28:45.1	56.54 $\pm$ 0.13	3.79 $\pm$ 0.28	58	9	0.23 $\pm$ 0.02	5.48*	6.18	Maser-RRL
G69.543-0.973	20:10:09.00	31:31:35.9	11.36 $\pm$ 0.21	4.66 $\pm$ 0.51	125	28	0.62 $\pm$ 0.06	2.46	7.62	Maser-only
G75.770+0.344	20:21:41.73	37:26:02.5	-1.08 $\pm$ 0.34	4.25 $\pm$ 0.88	29	11	0.13 $\pm$ 0.02	3.83	8.09	Maser-RRL
G81.752+0.591	20:39:02.01	42:24:59.3	-3.18 $\pm$ 0.07	2.87 $\pm$ 0.16	134	12	0.41 $\pm$ 0.02	1.50	8.05	Maser-RRL
G81.871+0.779	20:38:36.66	43:37:30.5	10.26 $\pm$ 0.04	3.56 $\pm$ 0.11	103	5	0.39 $\pm$ 0.01	1.30	8.04	Maser-RRL
G84.638-1.140	20:56:18.81	43:34:25.1	6.93 $\pm$ 0.06	0.49 $\pm$ 0.11	72	10	0.04 $\pm$ 0.01	1.34*	8.08	RRL-only
			8.37 $\pm$ 0.06	0.45 $\pm$ 0.14	46		0.02 $\pm$ 0.01			
G90.921+1.487	21:09:12.87	50:01:02.6	-67.82 $\pm$ 0.11	0.75 $\pm$ 0.20	65	20	0.05 $\pm$ 0.02	5.85	10.09	Maser-only
G92.670+3.072	21:09:21.22	52:22:35.7	-5.32 $\pm$ 0.13	3.02 $\pm$ 0.28	52	9	0.17 $\pm$ 0.01	1.63	8.36	RRL-only
G111.532+0.759	23:13:43.87	61:26:55.8	-55.7 $\pm$ 0.13	5.05 $\pm$ 0.30	97	13	0.52 $\pm$ 0.03	2.69*	9.45	Maser-RRL
G174.205-0.069	05:30:49.01	33:47:46.7	-2.41 $\pm$ 0.13	2.71 $\pm$ 0.31	34	6	0.10 $\pm$ 0.01	2.13*	10.24	Maser-only
G192.600-0.048	06:12:53.99	17:59:23.7	7.95 $\pm$ 0.17	3.02 $\pm$ 0.37	45	10	0.14 $\pm$ 0.02	1.66	9.76	Maser-only
G208.824-19.256	05:35:24.29	-05:08:30.7	12.04 $\pm$ 0.14	2.63 $\pm$ 0.28	35	7	0.10 $\pm$ 0.01	0.42*	8.10	RRL-only

**Notes.** (1): Source name; (2): Right ascension (J2000); (3): Declination(J2000); (4): LSR velocity; (5): Full width at half maximum (FWHM) ; (6): Peak  $T_{mb}$  value; (7): The rms noise value; (8): Integrated line intensity; (9): The heliocentric distance  $D$  is taken from the trigonometric parallax measurements (Reid et al. 2014, 2019). Others (with \*) are obtained from the latest Parallax-based Distance Calculator V2; (10): The galactocentric distance  $D_{GC}$ ; (11): Classifications.

**Table B.2.** The HC<sub>5</sub>N (J = 3-2) and HC<sub>7</sub>N(J = 15-14) transitions detected with TMRT.

Molecule	Source Name	R.A. (hh.mm.ss)	DEC (hh.mm.ss)	$V_{\text{LSR}}$ (km s <sup>-1</sup> )	$\Delta\nu$ (km s <sup>-1</sup> )	$T_{\text{mb}}$ (mK)	rms (mK)	$\int T_{\text{mb}} d\nu$ (K km s <sup>-1</sup> )	Classifications
(1)	(2)	(3)	(4)	(5)	(6)	(7)	(8)	(9)	(10)
HC <sub>5</sub> N	G20.234+0.085	18:27:44.56	-11:14:54.2	70.54±0.15	1.55±0.36	67	17	0.11±0.02	Maser-only
	G23.436-0.184	18:34:39.21	-08:31:40.4	101.97±0.15	1.05±0.43	47	13	0.05±0.02	Maser-RRL
	G24.328+0.144	18:35:08.15	-07:35:04.4	113.27±0.10	0.83±0.29	53	12	0.05±0.01	Maser-RRL
	G24.790+0.084	18:36:12.45	-07:12:10.7	109.06±0.06	3.41±0.13	47	3	0.17±0.01	Maser-RRL
	G28.393+0.085	18:42:50.49	-04:00:00.0	77.20±0.25	2.78±0.97	33	9	0.10±0.02	Maser-RRL
	G30.770-0.804	18:50:21.51	-02:17:27.5	78.83±0.18	1.57±0.49	34	11	0.06±0.01	Maser-only
	G30.810-0.050	18:47:46.97	-01:54:26.4	98.07±0.24	3.44±0.46	45	13	0.16±0.02	Maser-RRL
	G30.897+0.163	18:47:08.77	-01:44:12.7	105.45±0.16	1.47±0.43	30	9	0.05±0.01	Maser-RRL
	G35.141-0.750	18:58:06.14	01:37:07.5	34.97±0.17	1.19±0.49	60	19	0.08±0.02	Maser-RRL
	G81.752+0.591	20:39:02.01	42:24:59.3	-3.48±0.18	2.77±0.40	79	19	0.23±0.03	Maser-RRL
	G81.871+0.779	20:38:36.66	43:37:30.5	9.36±0.17	3.07±0.49	26	5	0.09±0.01	Maser-RRL
HC <sub>7</sub> N	G24.790+0.084	18:36:12.45	-07:12:10.7	109.98±0.35	3.55±1.05	8	3	0.03±0.01	Maser-RRL

**Notes.** (1): Molecules species; (2): Source name; (3): Right ascension (J2000); (4): Declination(J2000); (5): LSR velocity; (6): FWHM; (7): Peak  $T_{\text{mb}}$  value; (8): The rms noise value; (9): Integrated line intensity; (10): Classifications.

**Table B.3.** The column density and the relative abundance for  $\text{HC}_3\text{N}$ ,  $\text{HC}_5\text{N}$ , and  $\text{HC}_7\text{N}$ .

Classifications	Source Name	$T_{\text{rot}}$ (K)	$N(\text{HC}_3\text{N})$ ( $\times 10^{13} \text{ cm}^{-2}$ )	$X(\text{HC}_3\text{N})$ ( $\times 10^{-10}$ )	$N(\text{HC}_5\text{N})$ ( $\times 10^{13} \text{ cm}^{-2}$ )	$X(\text{HC}_5\text{N})$ ( $\times 10^{-10}$ )	$N(\text{HC}_7\text{N})$ ( $\times 10^{13} \text{ cm}^{-2}$ )	$X(\text{HC}_7\text{N})$ ( $\times 10^{-10}$ )	$N(\text{HC}_3\text{N})/N(\text{HC}_5\text{N})$	Reference
(1)	(2)	(3)	(4)	(5)	(6)	(7)	(8)	(9)	(10)	(11)
Maser-only	G20.234+0.085	15.11	$1.96 \pm 0.13$	$1.07 \pm 0.08$	$0.43 \pm 0.08$	$0.23 \pm 0.05$	...	...	4.55	1
	G23.484+0.097	16.10	$2.05 \pm 0.14$	$2.86 \pm 0.21$	...	...	...	...	...	2
	G25.649+1.050	20.60	$2.06 \pm 0.25$	$1.94 \pm 0.17$	...	...	...	...	...	3
	G28.817+0.365	18.96	$1.54 \pm 0.23$	$1.04 \pm 0.15$	...	...	...	...	...	2
	G30.770-0.804	17.56	$0.95 \pm 0.07$	$0.34 \pm 0.03$	$0.26 \pm 0.04$	$0.09 \pm 0.02$	...	...	3.64	2
	G37.043-0.035	15.22	$1.12 \pm 0.13$	$0.02 \pm 0.01$	...	...	...	...	...	2
	G69.543-0.973	21.20	$5.22 \pm 0.51$	...	...	...	...	...	...	3
	G90.921+1.487	18.90*	$0.39 \pm 0.16$	...	...	...	...	...	...	...
	G174.205-0.069	19.80	$0.80 \pm 0.08$	...	...	...	...	...	...	3
	G192.600-0.048	25.52	$1.37 \pm 0.20$	...	...	...	...	...	...	1
Maser-RRL	G23.271-0.256	18.62	$1.70 \pm 0.15$	$4.32 \pm 0.39$	...	...	...	...	...	2
	G23.389+0.185	16.80	$1.31 \pm 0.14$	$1.02 \pm 0.11$	...	...	...	...	...	3
	G23.436-0.184	17.27	$4.37 \pm 0.14$	$12.32 \pm 0.51$	$0.21 \pm 0.08$	$0.58 \pm 0.23$	...	...	20.81	4
	G23.965-0.110	22.36	$3.66 \pm 0.44$	$8.55 \pm 1.03$	...	...	...	...	...	2
	G24.328+0.144	13.31	$3.02 \pm 0.12$	$10.37 \pm 0.41$	$0.18 \pm 0.04$	$0.61 \pm 0.13$	...	...	16.78	5
	G24.528+0.337	11.22	$1.19 \pm 0.16$	...	...	...	...	...	...	6
	G24.790+0.084	22.01	$6.53 \pm 0.09$	$12.22 \pm 0.16$	$0.84 \pm 0.05$	$1.54 \pm 0.09$	$0.11 \pm 0.04$	$0.27 \pm 0.09$	7.77	1
	G25.709+0.044	18.30	$2.17 \pm 0.15$	$2.13 \pm 0.02$	...	...	...	...	...	3
	G28.147-0.004	18.67	$1.01 \pm 0.15$	$2.46 \pm 0.15$	...	...	...	...	...	2
	G28.287-0.348	13.62	$1.10 \pm 0.12$	...	...	...	...	...	...	5
	G28.393+0.085	11.30	$2.84 \pm 0.05$	$9.16 \pm 0.18$	$0.34 \pm 0.07$	...	...	...	8.35	7
	G29.835-0.012	20.10	$0.50 \pm 0.16$	$0.56 \pm 0.18$	...	...	...	...	...	3
	G30.810-0.050	22.00	$10.13 \pm 0.26$	...	$0.79 \pm 0.10$	...	...	...	12.82	2
	G30.897+0.163	18.49	$1.32 \pm 0.15$	$1.91 \pm 0.22$	$0.22 \pm 0.04$	$0.31 \pm 0.06$	...	...	6.00	2
	G31.579+0.076	23.80	$2.17 \pm 0.18$	$1.52 \pm 0.13$	...	...	...	...	...	3
	G35.141-0.750	20.05	$3.91 \pm 0.16$	$3.65 \pm 0.16$	$0.37 \pm 0.09$	$0.35 \pm 0.08$	...	...	10.57	2
	G35.194-1.725	19.09*	$1.18 \pm 0.16$	...	...	...	...	...	...	...
	G49.466-0.408	19.09*	$1.80 \pm 0.16$	...	...	...	...	...	...	...
	G75.770+0.344	32.60	$1.56 \pm 0.24$	...	...	...	...	...	...	3
	G81.752+0.591	18.60	$3.12 \pm 0.15$	...	$1.02 \pm 0.13$	...	...	...	3.06	3
	G81.871+0.779	19.09*	$3.06 \pm 0.08$	...	...	...	...	...	...	3
RRL-only	G111.532+0.759	23.60	$4.78 \pm 0.28$	...	...	...	...	...	...	...
	G24.546-0.245	17.96	$1.38 \pm 0.15$	$3.11 \pm 0.36$	...	...	...	...	...	2
	G28.452+0.002	17.96*	$0.67 \pm 0.07$	$0.18 \pm 0.02$	...	...	...	...	...	...
	G49.028-0.217	17.96*	$0.47 \pm 0.15$	...	...	...	...	...	...	...
	G84.638-1.140	17.96*	$0.59 \pm 0.07$	...	...	...	...	...	...	...
	G92.670+3.072	17.96*	$1.23 \pm 0.07$	...	...	...	...	...	...	...
	G208.824-19.256	17.96*	$0.72 \pm 0.07$	...	...	...	...	...	...	...

**Notes.** (1): Classifications; (2): Source name; (3): The rotational temperature of  $\text{NH}_3$ .  $T_{\text{rot}}$  value with \* shows the mean  $T_{\text{rot}}$  of each type; (4)-(9): The column density and relative abundance of  $\text{HC}_3\text{N}$ ,  $\text{HC}_5\text{N}$  and  $\text{HC}_7\text{N}$ ; (10): The abundance ration of  $N(\text{HC}_3\text{N})/N(\text{HC}_5\text{N})$ ; (11): The rotational temperature values are taken from: 1 (Yang et al. in prep.), 2 (Wienen et al. 2012), 3 (Urquhart et al. 2011), 4 (Li et al. 2016), 5 (Cyganowski et al. 2013), 6 (Svoboda et al. 2016) and 7 (Chira et al. 2013).

**Table B.4.** The integrated line intensities of other molecules.

Classifications	Source name	$I_{\text{H}_2\text{CO}}$ (K km s <sup>-1</sup> )	$N_{\text{H}_2\text{CO}}$ ( $\times 10^{13} \text{cm}^{-2}$ )	$I_{\text{SiO}}$ (K km s <sup>-1</sup> )	$N_{\text{SiO}}$ ( $\times 10^{13} \text{cm}^{-2}$ )
(1)	(2)	(3)	(4)	(5)	(6)
Maser-only	G30.770-0.804	1.11±0.09	0.82±0.07	...	...
	G37.043-0.035	...	...	1.23±0.12	0.22
	G69.543-0.973	3.51±0.07	8.75±0.17	...	...
	G174.205-0.069	1.18±0.09	0.77±0.06	...	...
Maser-RRL	G23.389+0.185	0.53±0.05	0.45±0.04	1.36±0.25	0.24
	G23.436-0.184	13.75±0.37	23.04±0.62	14.07±0.37	2.50
	G23.965-0.110	2.48±0.08	3.37±0.11	7.53±0.25	1.30
	G24.328+0.144	3.29±0.11	4.76±0.16	...	...
	G24.528+0.337	3.97±0.08	2.18±0.04	...	...
	G24.790+0.084	3.57±0.07	13.73±0.27	17.41±0.37	3.10
	G28.147-0.004	2.27±0.17	1.55±0.12	...	...
	G28.287-0.348	2.35±0.05	1.47±0.03	...	...
	G28.393+0.085	8.39±0.07	10.85±0.09	9.28±0.22	1.70
	G30.897+0.163	...	...	3.19±0.21	0.57
	G31.579+0.076	...	...	3.83±0.25	0.68
	G35.141-0.750	...	...	12.47±0.37	2.20
	G49.466-0.408	58.82±0.62	61.49±0.65	...	...
	G81.752+0.591	2.71±0.09	6.46±0.21	...	...
	G81.871+0.779	1.98±0.08	3.75±0.15	...	...
RRL-only	G24.546-0.245	1.43±0.08	1.42±0.08	...	...
	G28.452+0.002	2.55±0.11	1.48±0.06	...	...
	G49.028-0.217	1.01±0.07	0.82±0.06	...	...
	G92.670+3.072	0.72±0.05	0.64±0.04	...	...

**Notes.** (1): Classification; (2): Source name; (3): The integrated line intensity of H<sub>2</sub>CO (taken from TMRT C band survey); (4): The column density of H<sub>2</sub>CO, which is derived as done for cyanopolyynes in Sect. 3.1; (5-6): The integrated line intensity and column density of SiO, taken from Csengeri et al. (2016).

## Appendix C: Source catalogue without cyanopolyne detection

**Table C.1.** Sources without HC<sub>3</sub>N (J = 2-1) detection.

Source Name	R.A. (hh:mm:ss)	DEC (hh:mm:ss)	Classifications	rms (mK)
(1)	(2)	(3)	(4)	(5)
G20.749-0.112	18:29:21.28	-10:52:38.5	RRL-only	12
G23.009-0.379	18:34:33.43	-08:59:46.9	Maser-RRL	13
G23.010-0.410	18:34:40.25	-09:00:38.2	Maser-RRL	16
G23.338-0.213	18:34:34.42	-08:37:41.3	RRL-only	10
G23.428-0.231	18:34:48.38	-08:33:22.0	Maser-RRL	6
G23.653-0.143	18:34:54.65	-08:18:59.2	Maser-RRL	6
G23.680-0.189	18:35:07.46	-08:18:47.9	Maser-RRL	7
G23.899+0.065	18:34:37.20	-08:00:09.7	Maser-RRL	6
G24.010+0.503	18:33:15.42	-07:42:04.7	RRL-only	11
G24.148-0.009	18:35:21.02	-07:48:54.1	Maser-only	6
G24.313-0.154	18:36:10.51	-07:44:06.1	Maser-RRL	6
G24.362-0.146	18:36:14.34	-07:41:19.3	Maser-RRL	5
G24.485+0.180	18:35:17.92	-07:25:44.4	Maser-RRL	5
G24.564-0.308	18:37:11.55	-07:35:01.3	RRL-only	6
G24.633+0.153	18:35:40.11	-07:18:34.8	Maser-RRL	11
G24.818-0.108	18:36:56.84	-07:15:59.3	RRL-only	12
G24.943+0.074	18:36:31.49	-07:04:16.9	Maser-RRL	11
G25.177+0.211	18:36:28.20	-06:48:00.7	Maser-RRL	11
G25.346-0.189	18:38:12.83	-06:50:00.8	Maser-RRL	11
G25.395+0.033	18:37:30.44	-06:41:18.3	Maser-RRL	14
G26.545+0.423	18:38:14.50	-05:29:17.2	Maser-RRL	39
G26.579-0.120	18:40:14.60	-05:42:23.2	RRL-only	8

Source Name	R.A. (hh:mm:ss)	DEC (hh:mm:ss)	Classifications	rms (mK)
(1)	(2)	(3)	(4)	(5)
G26.645+0.021	18:39:31.66	-05:35:00.1	Maser-only	11
G27.220+0.261	18:40:03.69	-04:57:42.4	Maser-only	16
G27.287+0.154	18:40:34.11	-04:57:05.4	Maser-only	13
G28.832-0.250	18:44:50.45	-03:45:44.7	Maser-RRL	11
G28.855-0.219	18:44:46.41	-03:43:41.5	RRL-only	10
G29.320-0.162	18:45:25.16	-03:17:16.9	Maser-RRL	15
G30.392+0.121	18:46:22.34	-02:12:18.7	RRL-only	9
G30.902-0.035	18:47:51.61	-01:49:21.0	RRL-only	9
G31.101+0.265	18:47:09.28	-01:30:30.7	RRL-only	6
G33.641-0.228	18:53:32.57	00:31:39.2	Maser-only	6
G34.267-0.210	18:54:37.25	01:05:33.7	Maser-only	12
G35.067-1.569	19:00:55.11	01:11:02.9	RRL-only	9
G35.197-0.729	18:58:10.11	01:40:58.4	Maser-only	6
G37.430+1.517	18:54:14.38	04:41:40.3	Maser-only	8
G37.669-0.093	19:00:25.60	04:10:19.9	RRL-only	8
G37.873-0.399	19:01:53.53	04:12:50.3	RRL-only	6
G38.258-0.074	19:01:26.23	04:42:17.3	Maser-RRL	11
G43.076-0.078	19:10:22.05	08:58:51.5	Maser-RRL	10
G43.148+0.013	19:10:10.98	09:05:18.1	Maser-RRL	10
G45.070+0.124	19:13:23.60	10:50:34.7	Maser-only	8
G45.124+0.136	19:13:27.22	10:53:49.0	RRL-only	9
G45.493+0.126	19:14:11.36	11:13:06.4	Maser-only	10
G45.541-0.016	19:14:47.48	11:11:43.3	RRL-only	13
G48.946-0.331	19:22:27.89	14:03:24.8	RRL-only	8
G49.072-0.327	19:22:41.83	14:10:11.9	RRL-only	7
G49.224-0.334	19:23:01.07	14:18:00.5	RRL-only	10
G49.265+0.311	19:20:44.86	14:38:26.9	Maser-only	20
G49.391-0.235	19:22:59.18	14:29:41.1	RRL-only	7
G49.416+0.326	19:20:59.21	14:46:49.7	Maser-only	5
G51.341+0.065	19:25:43.12	16:21:14.1	RRL-only	11
G58.775+0.647	19:38:49.13	23:08:40.2	Maser-only	10
G59.634-0.192	19:43:50.00	23:28:38.8	Maser-only	15
G59.785+0.068	19:43:10.72	23:44:14.9	Maser-only	6
G75.841+0.425	20:21:33.82	37:32:21.4	RRL-only	6
G76.659+1.922	20:17:37.28	39:03:35.3	RRL-only	15
G78.881+1.427	20:26:19.99	40:36:11.0	RRL-only	7
G79.024+2.449	20:22:20.27	41:18:23.4	RRL-only	11
G79.170+0.396	20:31:36.70	40:13:59.5	RRL-only	11
G79.877+2.476	20:24:49.89	42:01:18.3	RRL-only	6
G80.862+0.383	20:37:01.02	41:34:56.9	Maser-RRL	11
G80.865+0.342	20:37:12.22	41:33:34.8	Maser-RRL	12
G80.939-0.127	20:39:25.98	41:20:01.5	RRL-only	7
G81.250+1.123	20:35:05.61	42:20:16.3	RRL-only	10
G81.252+0.982	20:35:42.50	42:15:16.9	RRL-only	14
G81.337+0.824	20:36:40.29	42:13:37.9	RRL-only	7
G81.683+0.541	20:39:01.04	42:19:52.7	RRL-only	8
G82.308+0.729	20:40:16.72	42:56:28.6	Maser-only	8
G84.649-1.089	20:56:08.33	43:36:54.5	RRL-only	7
G84.941-1.162	20:57:29.82	43:47:21.5	RRL-only	9
G84.951-0.691	20:55:32.50	44:06:10.2	Maser-RRL	13
G97.527+3.184	21:32:11.30	55:53:39.5	Maser-RRL	4
G110.196+2.476	22:57:29.78	62:29:45.1	Maser-only	5
G111.526+0.803	23:13:33.10	61:29:15.2	Maser-RRL	9
G123.035-6.355	00:52:10.97	56:30:58.8	Maser-only	20
G123.050-6.310	00:52:17.18	56:33:42.6	Maser-only	9
G126.645-0.786	01:22:59.95	61:51:30.3	RRL-only	12
G133.690+1.113	02:25:10.17	62:00:39.9	RRL-only	8
G133.716+1.207	02:25:39.71	62:05:24.0	RRL-only	8
G134.004+1.144	02:27:45.35	61:55:40.2	RRL-only	16
G150.525-0.930	04:03:01.58	51:22:31.7	RRL-only	5
G173.596+2.823	05:41:05.42	35:52:02.4	Maser-RRL	18

Source Name	R.A. (hh:mm:ss)	DEC (hh:mm:ss)	Classifications	rms (mK)
(1)	(2)	(3)	(4)	(5)
G213.706-12.602	06:07:46.82	-06:23:08.3	Maser-RRL	10
G213.752-12.615	06:07:48.79	-06:25:55.3	Maser-RRL	6

**Notes.** (1): Source name; (2): Right ascension (J2000); (3): Declination(J2000); (4): Classifications; (5): The rms noise value.